Int. J. of Precis. Eng. and Manuf.-Green Tech.
https://doi.org/10.1007/s40684-026-00860-2

Online ISSN 2198-0810
Print ISSN 2288-6206

REGULAR PAPER

Design and Manufacturing of a High-Speed Motorized Spindle: Engineering Challenges and Insights

Saif Ahmad Afridi[1] · Esra Yuksel[1,2] · Gilbert Rivera[3] · Seong-Wook Hong[3] · Erhan Budak[1]

Received: 2 September 2025 / Revised: 4 February 2026 / Accepted: 7 February 2026

Abstract

High-speed spindle systems operating above 20,000 RPM pose significant design challenges due to strongly coupled dynamic, thermal, and manufacturing constraints. Conventional design approaches either rely on simplified analytical models with limited physical fidelity or computationally expensive numerical simulations that hinder full-system optimization. This paper presents the development, optimization, manufacturing, and experimental validation of a 40,000 RPM electro-spindle using an integrated, multi-stage, multi-objective optimization framework. The proposed methodology combines fast analytical dynamic modeling with reduced-order thermal analysis and a Teaching–Learning-Based Optimization (TLBO) algorithm. Spindle dynamics are modelled using an analytical bearing formulation and a Timoshenko-beam representation of the shaft, solved via Receptance Coupling Substructure Analysis (RCSA) to enable rapid evaluation of stiffness, stability, and critical-speed constraints. Thermal behavior is captured using POD-based thermal modal simulations, significantly reducing computational cost while preserving the dominant thermal characteristics required for optimization. The optimization process is structured into two stages: fundamental optimization, which establishes the shaft–bearing–motor architecture, and optimization for manufacturing, which incorporates preload strategies, lubrication and cooling layouts, sealing concepts, and manufacturability constraints. The optimization strategy guided decisions on bearing selection (71909 CE Front, 71907 CE Rear), bearing locations, dimensions for auxiliary components like sleeves, locknuts, and tail length. Although mid-design stages were presented, the optimization-guided decisions on auxiliary components led to potential improvements of 7% in natural frequency and 11% in mass reduction. The optimized spindle was manufactured and experimentally tested. The measured dynamic (fundamental spindle FRF response in the 1000 Hz range) and thermal responses (thermal deformation of 29 μm) show good agreement with model predictions and design targets, confirming the effectiveness of the proposed framework. The results demonstrate that integrating fast, physically representative models with manufacturability-aware optimization enables efficient and reliable design of high-speed spindles under realistic industrial constraints.

Keywords High-speed Spindle · Spindle Design · Thermal Analysis · Spindle Dynamics · Design Guideline · Machine Tools

1 Introduction

High-speed spindle design requires extensive iterative analysis due to the conflicting requirements, especially above 20,000 RPM, where advanced subsystem integration becomes essential. A typical high-speed spindle above 20,000 RPM requires a built-in motor, super-precision angular contact ball bearings, oil-air or pressurized lubrication, a jacket-type cooling system, and a fully automated drawbar, in some heavy-duty applications with through-shaft cooling [1, 2]. Manufacturing such systems is costly and requires significant expertise. A titanium cutting high-speed spindle

"This paper was presented at PRESM2025"

✉ Erhan Budak
ebudak@sabanciuniv.edu

[1] Manufacturing Research Laboratory, Faculty of Engineering & Natural Sciences, Sabanci University, Istanbul, Turkey

[2] Dynamics & Control Department, IDEKO, Elgoibar, Basque Country, Spain

[3] Department of Mechanical System Engineering, Kumoh National Institute of Technology, 61 Daehak-ro (yangho-dong), Gyeongbuk 39177 Gumi, Korea

Published online: 31 March 2026

can have the same cost as an average 3-Axis CNC. Component costs increase rapidly with speed: the drawbar and shaft-cooling assembly may reach 30% of the total cost above 30,000 RPM, comparable to commercial units such as Step-Tec CoolCore (42,000 RPM) [3], Kessler DMS (40,000 RPM) [4], or IBAG HSC Aero series [5], while the motor is between 15 and 20%. Bearings typically constitute 5–10% of the cost, while lubrication and cooling systems each account for 5–15%. Repair and maintenance of high-speed spindles can also reach 30% of the initial cost. These values exclude auxiliary components (sleeves, spacers, seals, hydraulic/pneumatic channels, electronics), which add further complexity.

Figure 1 illustrates a high-speed spindle design similar to commercial units mentioned above. The electro-spindle employs two O-configured ACBB sets with a constant-preload mechanism, oil-air lubrication channels, cooling jackets around the bearings and motor, and a drawbar with through-coolant capability. As shown in Fig. 1, high-speed spindles rely on specialized components capable of withstanding demanding dynamic and thermal loads [1, 6]. Conventional locknuts and seals become insufficient; therefore, stepped sleeves, labyrinth seals, flingers/slingers, and balance rings are used [7]. These elements ensure stiffness, preload stability, effective sealing, and safe operation under high centrifugal loads. Their manufacturability and integration must be explicitly considered in the optimization for the manufacturing stage.

The high-speed spindle design process begins with defining performance targets and customer requirements [8], which determine the tool-holder interface and initial motor parameters such as maximum speed, torque, and power. These selections specify the cutting capability of the spindle and therefore guide the sizing of the shaft and bearings.

The determination of the maximum cutting scenario defines the initial shaft layout, including the selection of the smallest feasible bearing sizes and shaft diameters, while ensuring that the design satisfies critical-speed requirements, typically set to at least twice the maximum operating speed. These decisions form the core of the *Conceptual Design* stage. At this stage, it is essential to establish the minimum and maximum allowable bearing sizes and shaft lengths through static bearing analyses and critical-speed evaluations. The motor selection, bearing configuration, and shaft layout together constitute the *Fundamental Optimization* stage, establishing the primary static, dynamic, and thermal characteristics of the spindle.

Once minimum bearing sizes and shaft geometry are set, further optimization addresses conflicting dynamic and thermal constraints. In this stage, bearing arrangement, preload strategy, lubrication method, and cooling requirements must be refined iteratively. Additional manufacturability considerations arise from components such as stepped sleeves, spacers, locknuts, sealing systems, and drawbar mechanisms. These decisions constitute the *Optimization for Manufacturing* stage. A generalized 10-step spindle

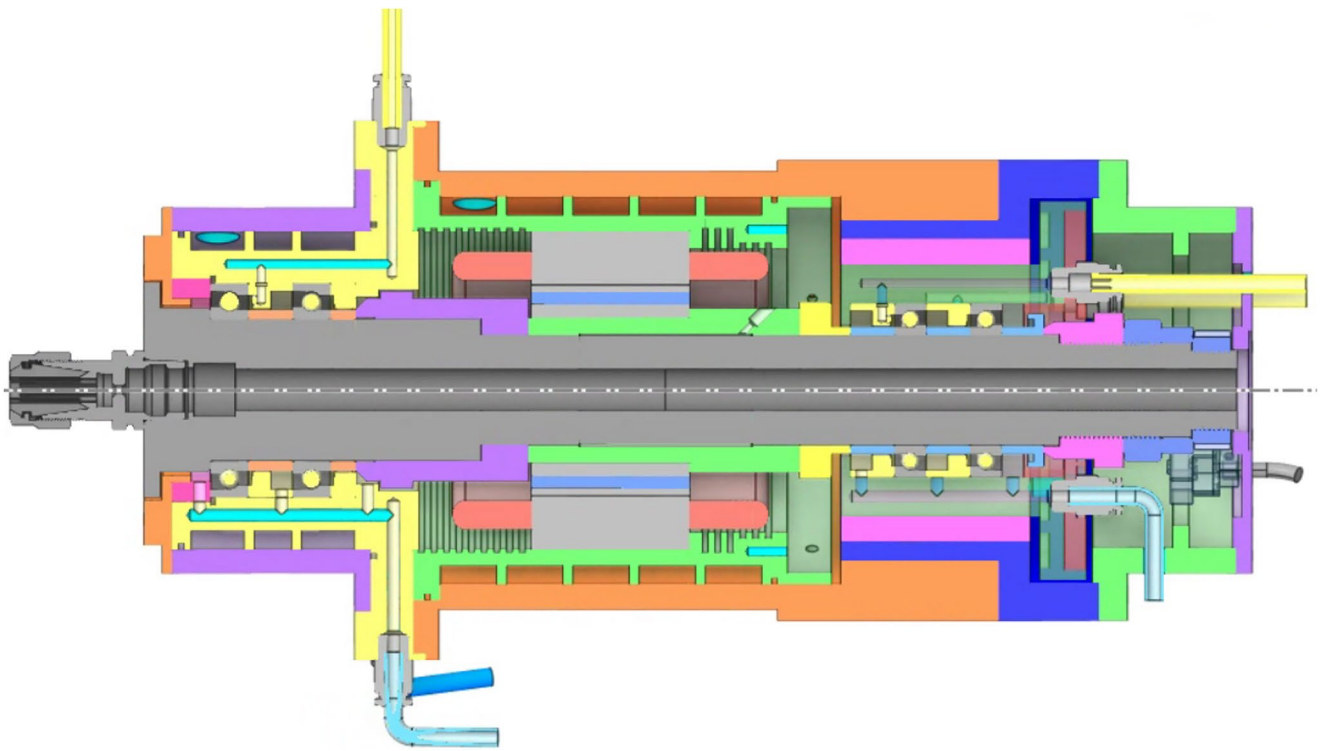

Fig. 1 A High-Speed Spindle Design for 40,000 RPM

design workflow summarizing both optimization phases is presented in Table 1.

There is a substantial body of literature on analytical and numerical modeling of machine-tool spindles [9–12]. These efforts primarily address the dynamic–thermal interaction in spindle–bearing systems. Analytical models offer speed but often oversimplify spindle physics, while numerical methods, especially finite element (FE), capture detailed behavior but require significant computational resources. This makes full system optimization impractical using FE alone.

Most published sensitivity studies focus on spindles below 20,000 RPM, which do not represent the dominant physical effects at higher speeds. Above this threshold, rotational inertia, centrifugal forces, and thermal gradients significantly influence bearing behavior, preload variation, rotor stability, and critical speeds. Even the simplest lubrication configuration must rely on oil–air injection, and integrated cooling systems become mandatory [1, 2]. Capturing these effects requires pre-stressed modal analysis, transient thermal simulations, and, in some cases, CFD for cooling and lubrication channels. These models are computationally intensive and, thus, become the primary bottleneck for spindle optimization.

Therefore, full spindle optimization requires fast yet physically realistic models capable of handling coupled thermal–dynamic effects that enable iterative design. It also requires an optimization engine capable of handling multiple objectives and constraints such as stiffness, temperature, dynamic stability, sustainability, and manufacturability while maintaining convergence robustness.

Although several papers provide generic optimization frameworks for spindle technologies focusing on considerations like thermal errors [13] and cooling strategies [14], systematic studies focusing specifically on high-speed spindle design, manufacturing, and testing remain scarce. Existing works typically address isolated subsystems (e.g., cooling optimization), but comprehensive multi-stage optimization frameworks that include manufacturability and validation are largely absent. Operational optimization, such as adaptive cooling control and energy-efficient spindle operation, is also seldom investigated due to its complexity and the cost of decoupled cooling systems. While some works present sensitivity analyses, no published study offers an integrated optimization methodology that covers dynamic, thermal, manufacturing, and operational aspects simultaneously.

In this work, the development and optimization of a 40,000 RPM spindle are presented together with insights obtained from its manufacturing and experimental testing up to 25,000 RPM. The optimization workflow includes both fundamental optimization and optimization for manufacturing. To the best of the authors' knowledge, no previous study has introduced such a comprehensive multi-objective optimization framework that integrates fast thermal and dynamic modeling with Teaching–Learning-Based Optimization (TLBO) and validates the results with a fully manufactured spindle.

The dynamic model employs an analytical bearing model combined with an analytical Timoshenko-beam representation of the spindle shaft. The dynamic response is calculated

Table 1 10-step spindle design plan

Task	Prerequisite →	Action →	Result	
1	Performance targets/customer requirements	Select toolholder/collet size	Shaft front geometry and maximum cutter diameter	a. Conceptual Design
2		Select motor parameters: maximum/nominal speeds, torque, power	Shaft size/length and bearing selection	
3		Select maximum cutting conditions	Maximum cutting loads	
4	Maximum cutting loads	Determine smallest possible bearing sizes and shaft dimensions	Shaft geometry	
5	Critical speed requirements (100,000 RPM)	Check minimum required shaft length for dynamic stability	Refined shaft geometry	
6	Tool holder and tool selection	Select drawbar	Shaft's internal geometry	b. Fundamental Optimization
7	Bearing selection	Select bearing arrangement and lubrication type	General shaft-bearing system definition	
8	Bearing arrangement selection	Determine preload mechanism	Refined shaft-bearing system definition	
9	Bearing lubrication system selection	Design the support infrastructure for the chosen lubrication system	Bearing lubrication channels, inlets/outlets, and selection of lubrication unit	c. Optimization for Manufacturing
10	Cooling system selection and requirements	Design cooling system for bearings and motor	Bearing and motor cooling channels, inlets/outlets, and selection of chiller unit	

using Receptance Coupling Substructure Analysis (RCSA) [15, 16], avoiding repeated FE solutions and enabling rapid optimization. Incorporating RCSA as the core dynamic solver within a spindle optimization framework is introduced here as a new contribution.

For thermal modeling, a reduced-order model based on a Proper Orthogonal Decomposition (POD)-based thermal modal analysis [17] is used to overcome the high computational cost of FE-based transient simulations. This approach provides realistic thermal predictions with a sufficiently sufficiently low computational load for integration into an optimization workflow. Incorporating thermal modal reduction into a spindle optimization engine represents another novel contribution.

Finally, the spindle is optimized not only for performance but also for manufacturability and operational feasibility. Sensitivity studies on dynamic and thermal metrics support these design decisions. The originality of the work lies in the modularization of key subsystems (cooling, lubrication, structural components), the development of a unified modeling and optimization framework, and the experimental validation of a fully manufactured spindle. The methodology provides a transferable template for high-speed spindle design under realistic industrial constraints.

This article is structured as follows. Section 2 introduces the spindle design and the methods. The spindle design requirements are defined, and the fast and accurate dynamic and thermal modeling methods used in the study are presented. In Sect. 3, the fundamental optimization stage and the optimization for manufacturing are then detailed. This section includes sensitivity analyses of the spindle's dynamic and thermal behavior. Section 4 discusses the spindle design evaluation together with the manufacturing process. Section 5 provides the experimental verification results obtained from the prototype spindle. Finally, Sect. 6 presents the conclusions.

2 Spindle Design & Modeling

2.1 Conceptual Design & Shaft Requirements

2.1.1 Conceptual Design

The conceptual design was guided by the performance metrics of a benchmark 40,000 RPM commercial milling spindle with a cooling unit, whose design parameters and experimental test results were available. This reference system, hereafter called the Base Spindle, is shown in Fig. 2a. Additional principles such as compactness, modularity, and sustainability were also considered. Table 2 summarizes the resulting design requirements, and the dynamic and thermal

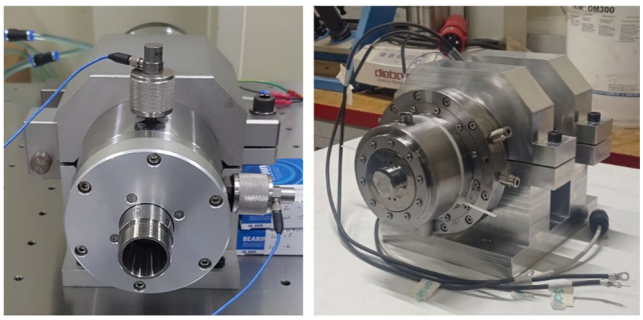

Fig. 2 **a**) Base spindle, **b**) MRL-40 K

Table 2 Performance targets

Quality	Attribute	Targets
Spindle Performance	Target Speed	40,000 RPM (Bearing Diameter: 45 mm)
	1st Critical Speed	> 100,000 RPM
	Dynamic Performance	Dominant FRF Modes > 1000 Hz (Base Spindle)
	Thermal Stability	Thermal Expansion at Spindle-Tip < 35 µm (Base Spindle)
	Radial Runout	< 20 µm
	Bearing Temperatures	< Manufacturer Limits (~40 °C)
Sustainability	Modularity	Separate Units for Distinct Thermal Zones
Efficiency	Compactness	Weight Minimization and Low Length-to-Width Ratio

targets were derived from the experimental performance of the Base Spindle. The optimized spindle developed in this study, referred to as the Manufacturing Research Laboratory 40,000 RPM (MRL-40K) spindle, is shown in Fig. 2b.

The study followed three stages: conceptual design, optimization, and manufacturing. The conceptual design began with a broad design space and was subsequently refined through literature review and benchmarking of commercial high-speed spindles. This process led to four core decisions:

- **Integrated motor**: Enables high-speed operation with reduced rotor inertia [1]. An interior permanent-magnet (IPM) motor was preferred due to its high-speed durability, offering 40,000 RPM capability with 11 Nm torque on a 540 V DC bus. The power and torque requirements were computed for a sample cutting case of Titanium with a 13 mm tool [18].
- **ACBB bearings**: Super-precision bearings for combined radial and axial loads [19].
- **Back-to-back configuration**: Provides higher axial and moment stiffness [19].

- **Constant spring preload**: Maintains stable preload under thermal expansion, with fixed front bearings and floating rear bearings [19]. It is acknowledged that while this choice introduces flexibility in the axial direction due to the usage of spring elements, it also offers improved thermal robustness compared to fixed displacement preload. In high-speed operation, where bearing heating and thermally induced preload variations can become critical, spring preload is commonly preferred in industrial practice to reduce the risk of overheating and premature bearing failure.

The conceptualization stage process involved the selection of fundamental spindle components, which ultimately provided the necessary constraints to draft the shaft-bearing system. The main components are discussed as follows:

The conceptual design stage begins with selecting the key spindle components, as these define the constraints for the shaft–bearing layout. The first decision is the toolholder. HSK 25E was chosen instead of BT/CAT systems because its internal clamping fingers provide better stability at high speeds, and it supports tool diameters up to 13 mm. With the tool and motor defined, the maximum cutting forces were estimated using the analytical model in [18], confirming that the motor meets the expected titanium-cutting load for a 13 mm tool.

2.1.2 Shaft Requirements and Critical Speed

The spindle design starts with the determination of the minimum bearing diameters, and for the determined specifications, it must be at least 40 mm for front bearings and 25 mm for the rear bearings [20]. According to these diameters, the critical length must be around 350 mm to ensure a critical speed of around 100,000 RPM. To determine the maximum bearing diameters with respect to the calculated spindle length, rotary dynamics simulations are used. Spindle design must account for high-speed dynamic effects like inertial, gyroscopic, and whirl. Gyroscopic moments, arising from rotor precession, can critically affect system stability and must be modelled accurately to avoid damage to bearings and supports. Stability depends on both bearing stiffness and support flexibility, which together influence the system's damping behavior.

The Finite Element (FE) model in Fig. 3 was constructed to represent the speed-dependent dynamics of the Base Spindle for verification purposes. Campbell diagrams were generated in ANSYS to evaluate modal frequencies under operational speeds, incorporating speed-dependent stiffness and gyroscopic effects. This functional FE model was then parameterized and used to construct an optimization problem to meet the 1st critical speed criteria set in Table 2.

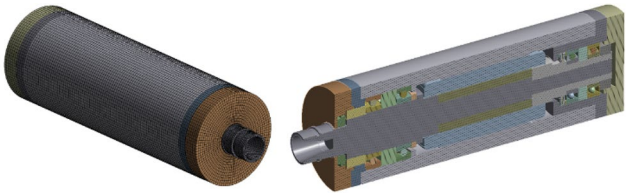

Fig. 3 FE model for critical speed analysis

Parameter Name	Lower Bound (mm)	Upper Bound (mm)	Driving Dimension (mm)
Motor Shaft	15	40	20.75
Front Bearing	20.25	24.75	22.5
Front Section	19.35	23.65	21.5
Rear Section	16.65	20.35	18.5
Rear Bearing	13.5	16.5	15

Fig. 4 Optimization problem formulation according to critical speed design criteria

Table 3 Optimal design alternatives for critical speed criteria

Parameter	Candidate Points 1	Candidate Point 2	Candidate Point 3
P1-Motor shaft (mm)	27.033	28.278	17.121
P2-Front bearing shaft (mm)	23.813	21.979	22.635
P3-Front section (mm)	21.542	20.435	22.655
P4-Rear shaft (mm)	16.911	17.69	17.556
P5-Rear bearing shaft (mm)	15.594	13.576	15.101
P10 – Mode 1 (RPM)	99,987	100,011	100,011

Figure 4 shows the design variables and their constraints for this optimization problem. Some geometric constraints, like the motor rotor's maximum radius, were derived from practical constraints. The gradient-based Adaptive Single Objective Method was used to solve this problem.

2.1.3 Optimization Results First Critical Speed (100,000 RPM)

The optimization results are shared in Table 3. The parametric optimizer searched for 100 design points, which showed the feasible front (CP 1) and rear bearing diameters (CP 2) for a given motor rotor size (CP 3). For this case, it showed that for a 27 mm rotor inner radius, a 40 mm diameter-sized front bearing, and a 30 mm rear bearing to be feasible. However, a reduced rotor diameter of 25 mm was also possible with an increased rear bearing diameter of 40 mm. These findings provided numerous viable options for refining the shaft design in the next stages.

2.2 Modeling Approach

The interdependent dynamic and thermal behaviors of high-speed spindles are a well-studied topic in the literature [1]. Therefore, based on these studies, a modular, integrated modeling approach was developed to accurately predict these behaviors. To the authors' knowledge, this combination has not yet been leveraged in multi-objective optimization frameworks for spindle design.

2.2.1 Dynamic Modeling

Spindle dynamic analysis mainly comprises bearing and shaft dynamics. The system response depends on bearing type, preload, shaft dimensions, and other structural elements. In this work, bearing stiffness was computed using a 5-DOF ACBB quasi-static model [7], while the shaft response was computed using the Timoshenko beam theory to obtain closed-form end receptances. These receptances were coupled using Receptance Coupling Substructural Analysis (RCSA) to assemble the dynamic model, enabling rapid prediction of the spindle tip FRF without repeated FE evaluations. The following sections briefly explain these analytical models, where only the representative equations are shared for brevity. The complete details of this approach can be found in our previous work [7].

The Bearing Module The bearing model [7] solves the fundamental bearing loading equation (Eq. 1) based on the non-linear Hertzian contact theory, considering gyroscopic/centrifugal terms. It computes the 5 × 5 bearing stiffness matrix (Eq. 2), providing the necessary inputs for further dynamic analyses in the form of translation, rotational, and cross-stiffness terms.

$$F = K_{\text{bearing}} \cdot \delta \tag{1}$$

$$K_{\text{bearing}}^{(5\times 5)} = \begin{bmatrix} K_{xx} & K_{xy} & \cdots & \cdots & \cdots \\ K_{yx} & K_{yy} & \cdots & \cdots & \cdots \\ & & \ddots & \cdots & \cdots \\ & & \cdots & K_{\theta_x\theta_x} & K_{\theta_x\theta_y} \\ & & \cdots & K_{\theta_y\theta_x} & K_{\theta_y\theta_y} \end{bmatrix} \tag{2}$$

Receptance Coupling Substructural Analysis The Receptance Coupling Substructural Analysis (RCSA) method [16] requires the shaft to be divided into substructures with distinct geometric dimensions, which are then analytically coupled after computing their individual dynamic receptances using the Timoshenko beam theory to obtain the shaft-tip FRF. The bearings introduce stiffness to the system, with the relevant bearing stiffness terms acquired from Eq. 2. The details of the RCSA algorithm are provided in [7], and an illustrative summary with the core algorithm flow and equations is shared in Fig. 5.

Figure 6 presents a comparison of the RCSA with the experimental FRF results for the Base Spindle.

2.2.2 Thermal Modeling

Efficient simulation of transient heat transfer is critical for applications in high-speed spindles where different fluidic and pneumatic systems effects need to be explored. Traditional finite element methods (FEM) become computationally expensive for such large-scale transient thermos-fluidic problems. In this study, the thermal analysis of the spindle is

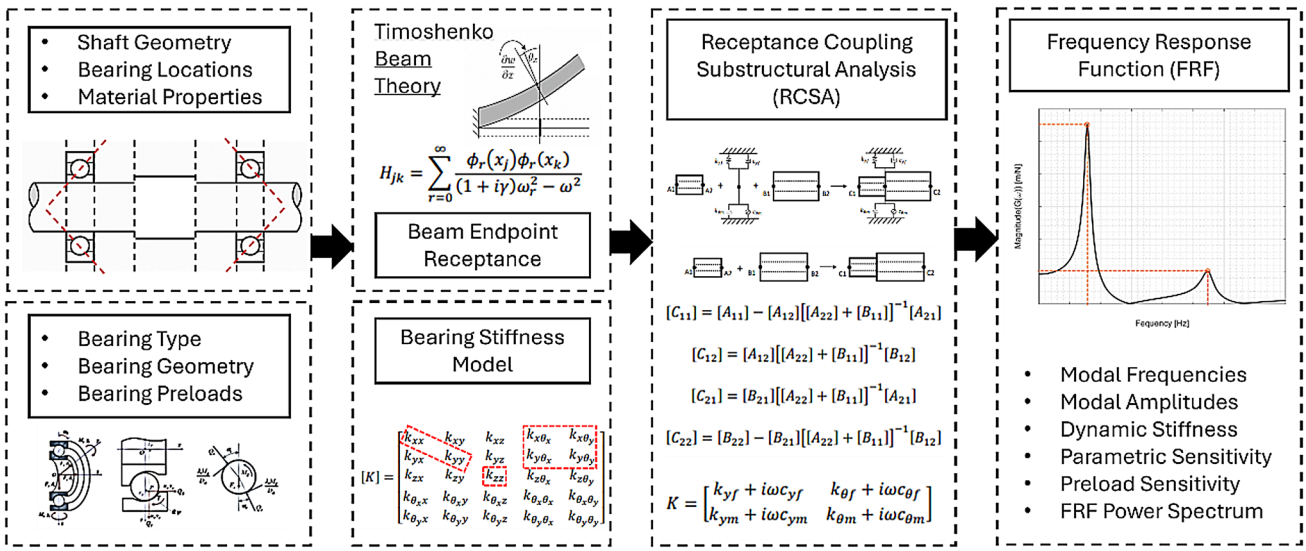

Fig. 5 Dynamic Modeling with the Bearing Module and RCSA algorithm

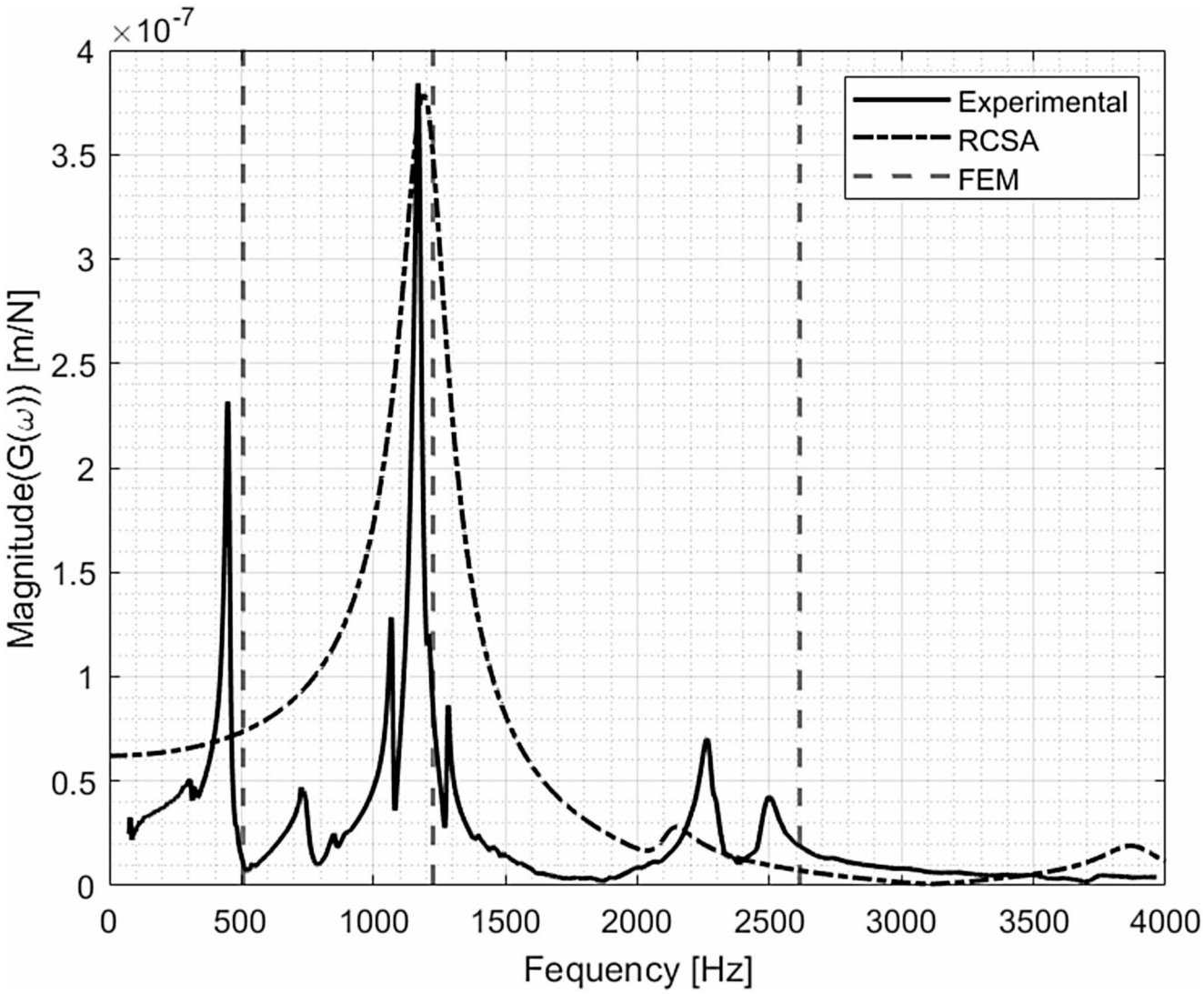

Fig. 6 Analytical dynamics prediction vs. experimental result (Base Spindle)

done by using a Proper Orthogonal Decomposition (POD) based thermal-modal analysis [17, 21].

-ThermalModal Analysis

The central premise of thermal modal analysis lies in representing the temperature field as a superposition of spatial modes, each associated with characteristic temporal behavior. These modal decompositions facilitate significant model order reduction (MOR), enabling fast yet accurate approximations of transient thermal responses. Traditionally, thermal modal analysis derives its modes from the eigenvalue problem associated with the heat conduction equation. Consider the linearized heat conduction equation in discretized form [21]:

$$\mathbf{C}\frac{d\mathbf{T}}{dt} + \mathbf{K}\mathbf{T} = \mathbf{F}(t) \tag{3}$$

where $\mathbf{C}$ is the heat capacity matrix, $\mathbf{K}$ the thermal conductivity (stiffness) matrix, and $\mathbf{T}$ the temperature vector. By solving the associated generalized eigenvalue problem,

$$\mathbf{K}\phi_i = \lambda_i \mathbf{C}\phi_i \tag{4}$$

a set of orthogonal thermal modes ϕ_i is obtained. These modes correspond to spatial eigenfunctions that decay exponentially with time, governed by eigenvalues, λ_i. The thermal field can then be expressed as a linear combination of these modes:

$$\mathbf{T}(t) \approx \sum_{i=1}^{r} q_i(t)\,\phi_i \tag{5}$$

where $q_i(t)$ are the modal amplitudes are determined through modal superposition.

In contrast to this physics-based formulation, Proper Orthogonal Decomposition (POD) offers a data-driven alternative for extracting dominant spatial patterns from thermal fields. POD does not require explicit knowledge of the governing equations; instead, it utilizes a series of solution snapshots $\{\mathbf{T}_j\}_{j=1}^{M}$ obtained either from high-fidelity simulations or experimental measurements. These snapshots are organized into a data matrix $\mathbf{X} \in \mathbb{R}^{N\times M}$, where each column corresponds to a thermal state at a given time. The POD modes are obtained by solving the eigenvalue problem associated with the correlation matrix [17]:

$$\mathbf{R} = \mathbf{X}^T\mathbf{X},\ \mathbf{R}\mathbf{v}_i = \lambda_i \mathbf{v}_i, \tag{6}$$

and reconstructing the spatial modes as:

$$\phi_i = \frac{1}{\sqrt{\lambda_i}}\mathbf{X}\mathbf{v}_i. \tag{7}$$

These POD modes form an orthonormal basis that optimally captures the energy content (in the least-squares sense) of the dataset. A reduced-order representation of the temperature field can then be expressed as in Eq. 8, with time-dependent coefficients, $a_i(t)$, obtained via projection.

$$(t) \approx \sum_{i=1}^{r} a_i(t)\,\phi_i, \tag{8}$$

Although the derivation mechanisms differ, both classical thermal modal analysis and POD share the common objective of dimensionality reduction through modal decomposition. Consequently, POD is frequently regarded as a form of thermal modal analysis, particularly in literature addressing reduced-order modeling (ROM) of thermal systems. The distinction lies in the origin of the basis: classical thermal modes are physically grounded in the system's governing equations, whereas POD modes are empirically derived from data. Nonetheless, in linear and time-invariant settings, POD modes often exhibit striking similarity to the physical modes, especially when the snapshot data span the dominant dynamics of the system. On the other hand, pure thermal modal analysis gives many insignificant modes and does not mark the significant modes [17].

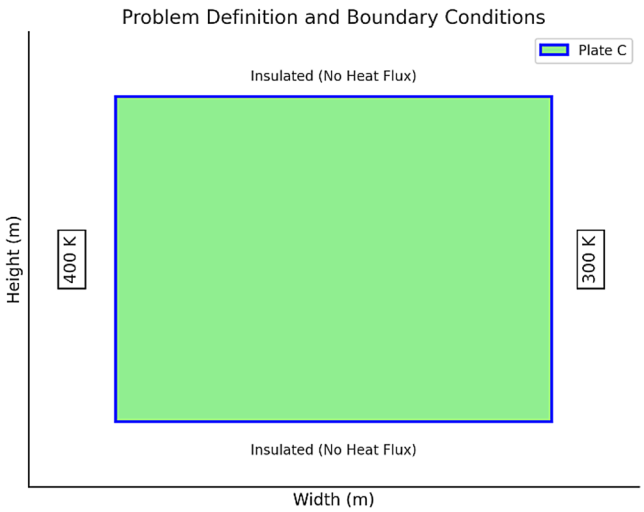

Fig. 7 Thermal System with Boundaries

A simple heat transfer problem is defined for demonstration and comparison purposes for the mentioned differences. First, one-plate problems with the same boundary conditions are solved as a thermal modal problem and a classical full transient fem solution. Therefore, in this section, we will present three different cases to compare for the same thermal problem.

A two-dimensional rectangular domain with a width $L_x = 1\,\mathrm{m}$ and a height $L_y = 1.0\,\mathrm{m}$. The plate material is characterized by thermal conductivity of $k = 205\,\mathrm{W/m^2\,K}$, a density of $\rho = 2700\,\mathrm{kg/m^3}$, and a specific heat capacity of $c_p = 900\,\mathrm{J/kg.\,K}$ For numerical analysis, the plate is discretized using a uniform finite element mesh consisting of $N_x = 10$ divisions along the width and $N_y = 10$ divisions along the height. This discretization provides a structured grid suitable for the finite element formulation of the heat conduction problem.

Based on the boundary conditions given in Fig. 7 and Fig. 8, the results are compatible with the boundary conditions which were constant at 400 K at right edge while the left edge stays 300 K as the Dirichlet boundary conditions while upper and lower edges insulated, and ambient temperature is 300 K. The temperature at 1220 s, is 400 K for the right-hand side and gradually decreased to 300 K at the left-hand side. Similar results have been obtained with pure thermal modal analysis and POD-based modal analysis. If the first 12 thermal modes are examined from pure thermal modal analysis, it can be observed that some modes are exactly matching with the modes obtained by POD-based thermal modal analysis, as indicated in Fig. 9.

In this simple plate problem, the number of thermal modes obtained by the pure thermal modal solution was set to 50. However, it is possible to represent the entire system with only 3 significant modes selected by POD-based thermal modal analysis as shown in Fig. 9. Since the spindle thermal model contains complex model details such as cooling, lubrication and pneumatic systems which are more intricate than modeling a plate, the POD-based thermal modal analysis is used in this study, and the reduced models are used for sensitivity analysis and optimization of the entire system.

-Thermal Modeling of the Spindle with Fluidic and Pneumatic Systems

Modeling Approach:

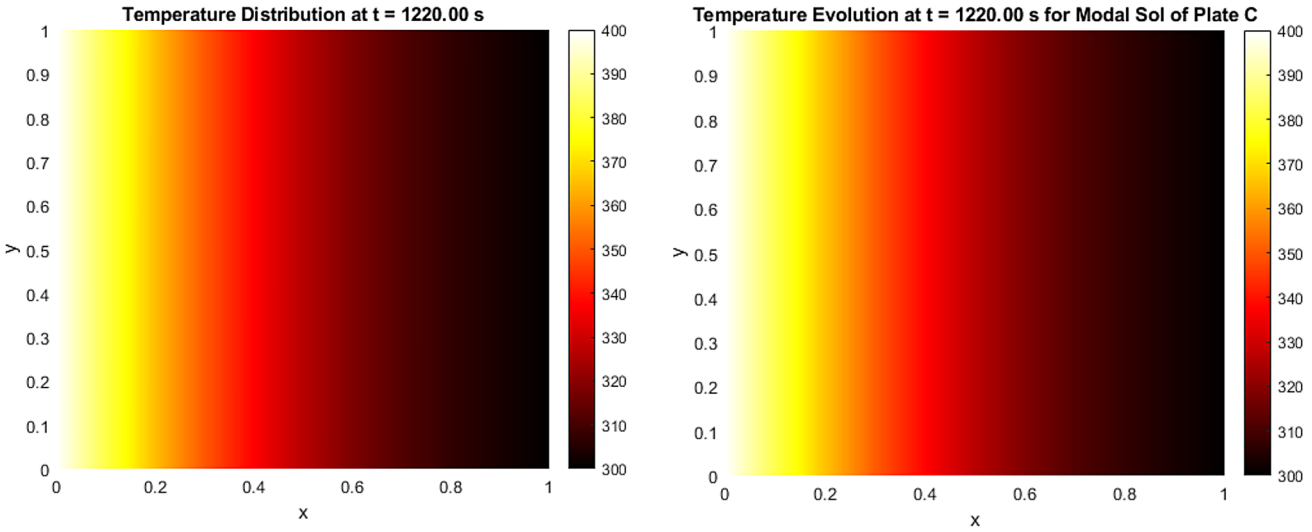

Fig. 8 Temperature distribution for Full-FEM and Thermal Modal solution at 1220 s

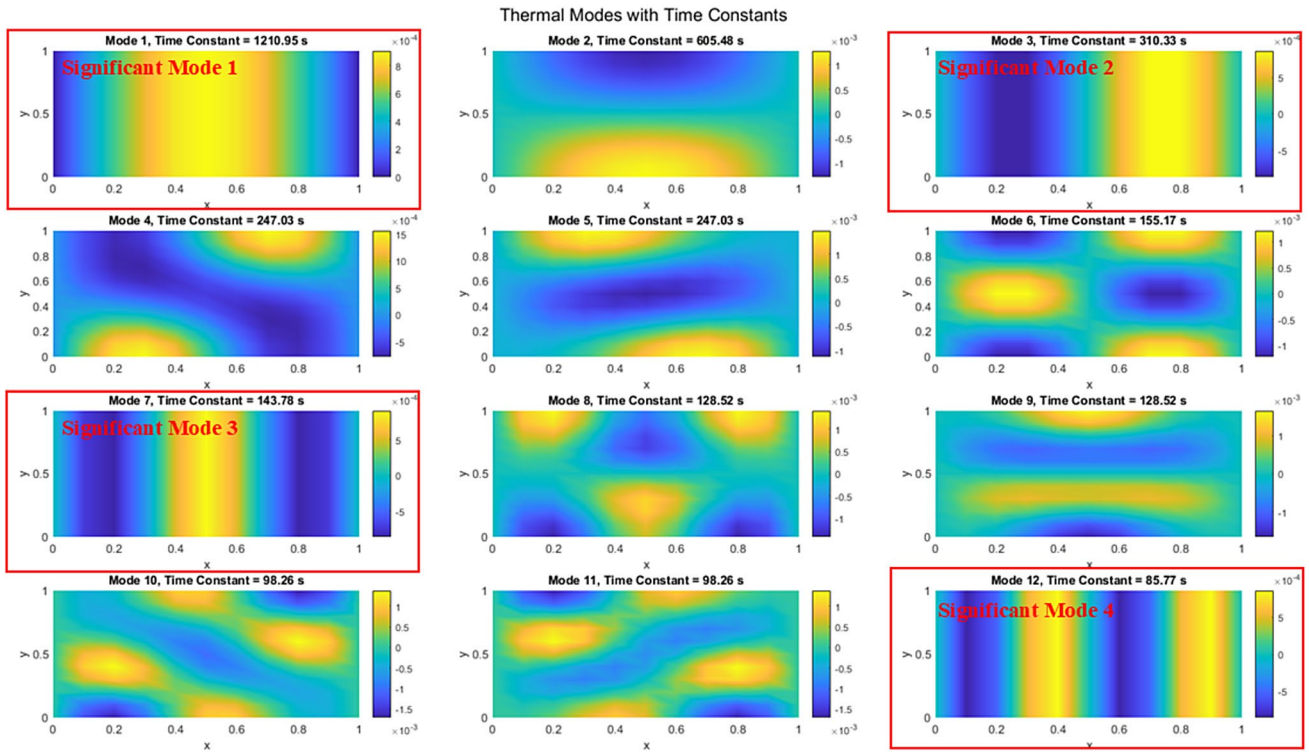

Fig. 9 Thermal Modes of Plate by pure and POD-based thermal modal analyses

The thermal behaviour of a high-speed spindle is governed by a strong interaction between solid heat conduction, internal cooling channels, and pneumatic lubrication and purge flows. A detailed high-speed spindle FE model consists of heat sources: cutting process-related, bearings, and a built-in motor. The heat sinks in a high-speed spindle include bearing and motor cooling water, pneumatic lubrication, purge flows, and ambient air.

For thermal loading conditions that enclose the time-dependent behaviour of.

1. Bearing heat generation due to friction and spin.
2. Heat loss of the built-in motor.
3. Contact conduction of bearing balls.
4. Forced-air convection of rotating cylinders.
5. Conduction between stationary components.
6. Free-air convection.

7. Bearing and Motor cooling jacket.
8. Pneumatic lubrication of bearings.
9. Purge Flows of the motor cooling chamber and labyrinth seals.

The thermal modeling details of the thermo-mechanical spindle modeling until the 6th part can be found in Ref. [7]. The modeling of internal cooling channels, pneumatic lubrication and purge flows will be explained in this section. By considering these fluidic and pneumatic systems, a fully resolved three-dimensional conjugate CFD–thermal analysis for all operating conditions would be computationally costly and unsuitable for design iteration and optimization even using POD-based thermal modal analysis.

Therefore, a reduced-order conjugate modeling strategy was adopted. In this approach, Computational Fluid Dynamics (CFD) is employed selectively to characterize flow-induced heat transfer phenomena that cannot be captured reliably by simplified correlations. The resulting thermal quantities are then transferred to a transient thermal finite element model implemented in ANSYS Mechanical, where fluid effects are represented through 1D thermal-fluid elements and equivalent convection boundary conditions. This strategy enables accurate prediction of spindle temperature fields while maintaining computational efficiency and physical interpretability.

CFD simulations are used to resolve the detailed flow physics in regions where local three-dimensional effects dominate heat transfer, namely: helical cooling channels inside the spindle shaft, oil–air lubrication outlets near the bearings, and pneumatic purge flows at labyrinth seals and motor cavities. Rather than solving the entire spindle thermal problem within the CFD environment, the CFD results are post-processed to extract equivalent thermal parameters that can be reused in the POD-based thermal modal analyses. The primary CFD outputs employed in the subsequent thermal analysis are:

- Local or segment-averaged heat transfer coefficients, $h\,(\mathrm{x},\mathrm{t})$,
- Bulk or reference fluid temperatures, $T_{\mathrm{bulk}}\,(\mathrm{x},\mathrm{t})$,
- Segment-wise UA values representing the integrated heat transfer capacity of cooling passages.

These quantities are mapped onto the thermal finite element model as boundary conditions.

Helical cooling channels:

The cooling system consists of a single-path helical channel embedded within the spindle shaft. Since the flow does not branch or merge, the bulk flow behaviour is predominantly one-dimensional, and axial temperature variation dominates over cross-sectional gradients. Under these conditions, the cooling channel is well-suited for 1D thermal-fluid modeling. The helical channel is represented using 1D thermal-fluid line elements (beam/pipe formulation). The channel is discretized into multiple axial segments, each satisfying the steady-state energy balance [22]:

$$\dot{m}c_p\frac{dT_b}{dx} = h\,(x)\;P\;[T_s\,(x) - T_b\,(x)] \tag{9}$$

where $\dot{m}$ is the mass flow rate, c_p is the specific heat capacity, T_b is the bulk fluid temperature, T_s is the local solid surface temperature, and P is the wetted perimeter. Heat exchange between the fluid and the surrounding solid is enforced via convection boundary conditions applied to the channel wall surfaces. The convection coefficient $h\,(x,t)$ and the bulk temperature $T_b\,(x,t)$ are obtained either from CFD or from validated correlations. This approach effectively captures conjugate heat transfer effects without solving the Navier–Stokes equations in the thermal model.

In Fig. 10, the CFD modeling of front bearing cooling channels is shown. The CFD results indicate the inlet and outlet temperatures and changing convection coefficients with respect to distance and time. To verify the proposed thermal FE framework, the temperature distribution was predicted for the Base Spindle with the cooling system. The proposed thermo-mechanical [7] model was used for predicting heat generation for the front bearings (SKF 7009 CE/HCP4BGV275) and rear bearings (SKF 7006 CE/HCP4BGV275). For the transient analysis, different speeds from 5000 RPM to 20,000 RPM were studied. The analysis results are shared in Fig. 11 for different spindle speed cases.

Similarly, the captured transient thermal growth behaviour of the spindle at different spindle speeds from the proposed FE framework is shared in Fig. 12.

Pneumatic and oil–air lubrication channels:

The pneumatic system includes oil–air lubrication and purge channels with characteristic diameters on the order of 3 mm. These channels, shown in Fig. 13, operate at relatively high velocities and discharge into confined regions near bearings and labyrinth seals, producing jet-dominated forced convection. Although oil is present, the mass fraction of oil is small, and the heat transfer process is dominated by the air phase. Consequently, the flow is modeled as a single-phase air flow for thermal purposes.

Each lubrication or purge outlet is modeled as an independent 1D thermal-fluid element, with a prescribed mass flow rate $\dot{m}$, specified inlet temperature, and adiabatic flow along the channel length. At the channel exits, the air jet impinges on nearby surfaces, producing localized forced convection at front bearings, rear bearings, motor bearings, and labyrinth seals. To represent this effect, a jet-based

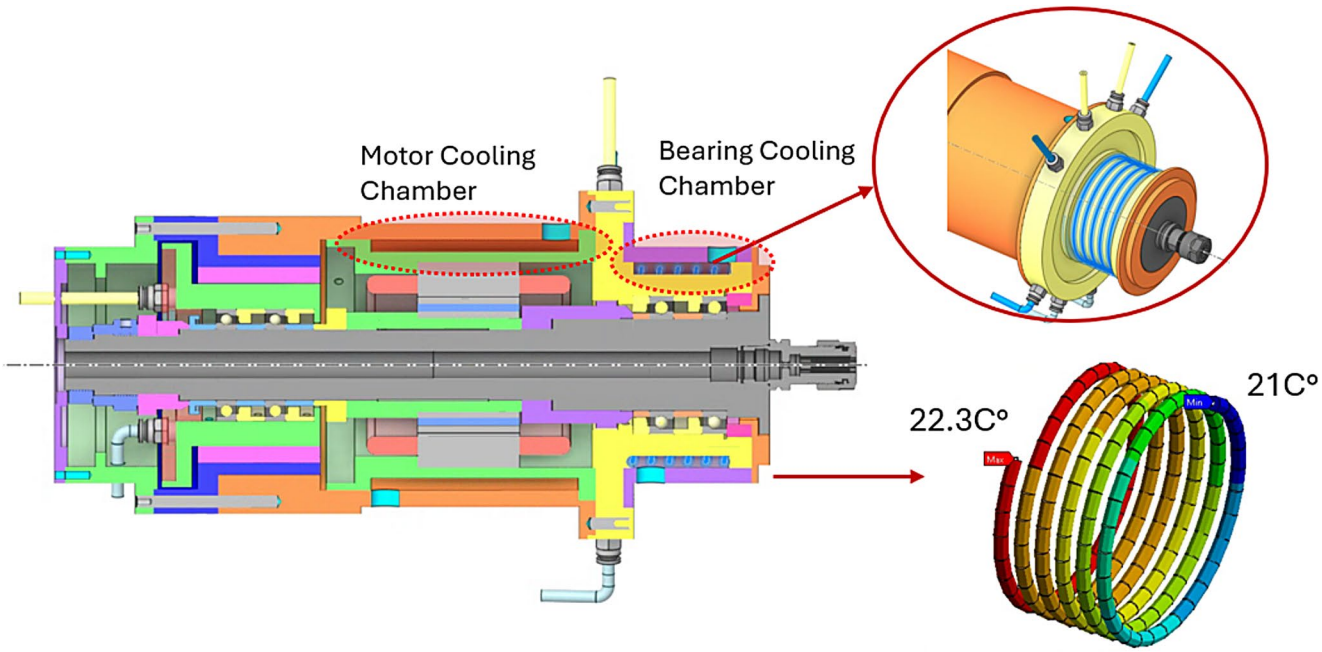

Fig. 10 The front cooling CFD results

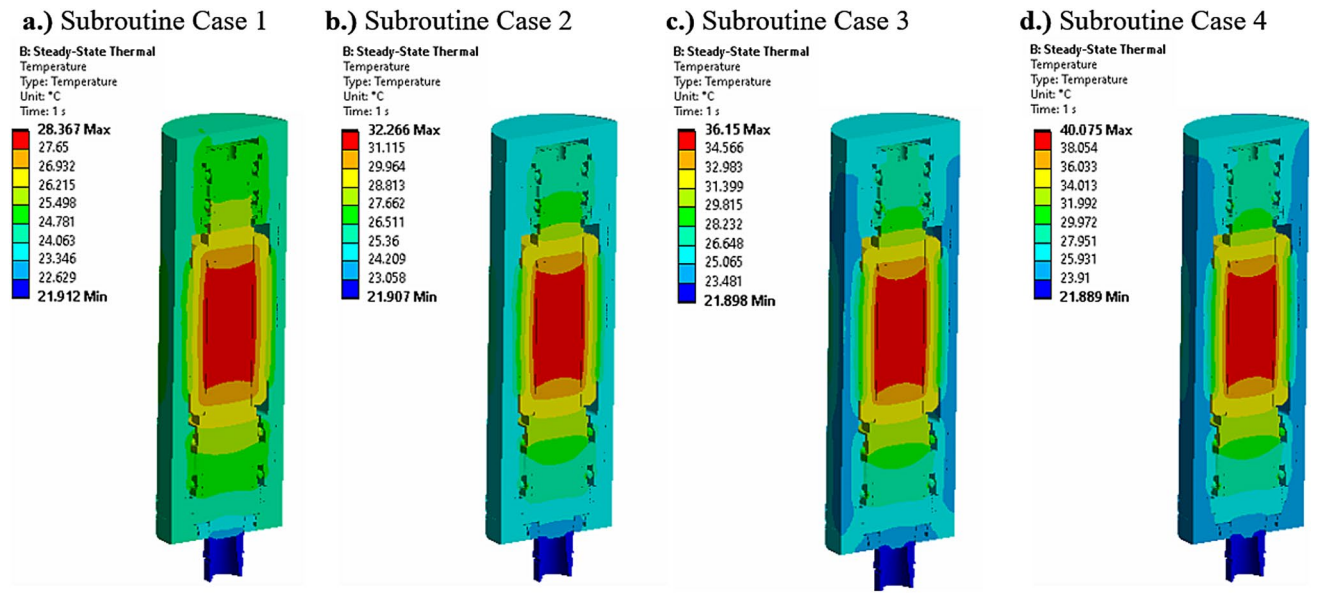

Fig. 11 Thermal FE results (Base Spindle)

forced convection model was derived using an engineering correlation of the form [22]:

$$Nu = C\, Re^{0.6}\, Pr^{1/3} \tag{10}$$

which leads to the scaling:

$$h\,(\dot{m}, D) \;\propto\; \dot{m}^{0.6}\, D^{-0.4} \tag{11}$$

where D is the characteristic diameter of the surface exposed to the jet, which can be parametrized during the design studies. This formulation enables a consistent and physically grounded determination of convection coefficients as a function of mass flow rate and geometric scale. In ANSYS Mechanical, bearing and labyrinth surfaces are assigned convection boundary conditions using the previously CFD-derived h-values. Depending on the analysis objective, the convection coefficient may be fixed for a single operating point, defined parametrically as a function

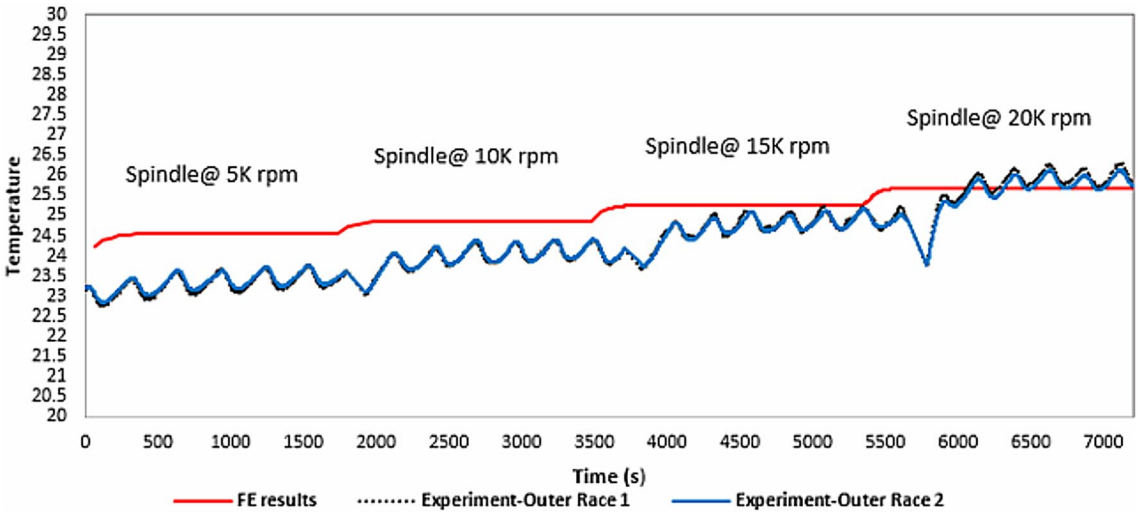

Fig. 12 Transient FE predictions vs. experiment

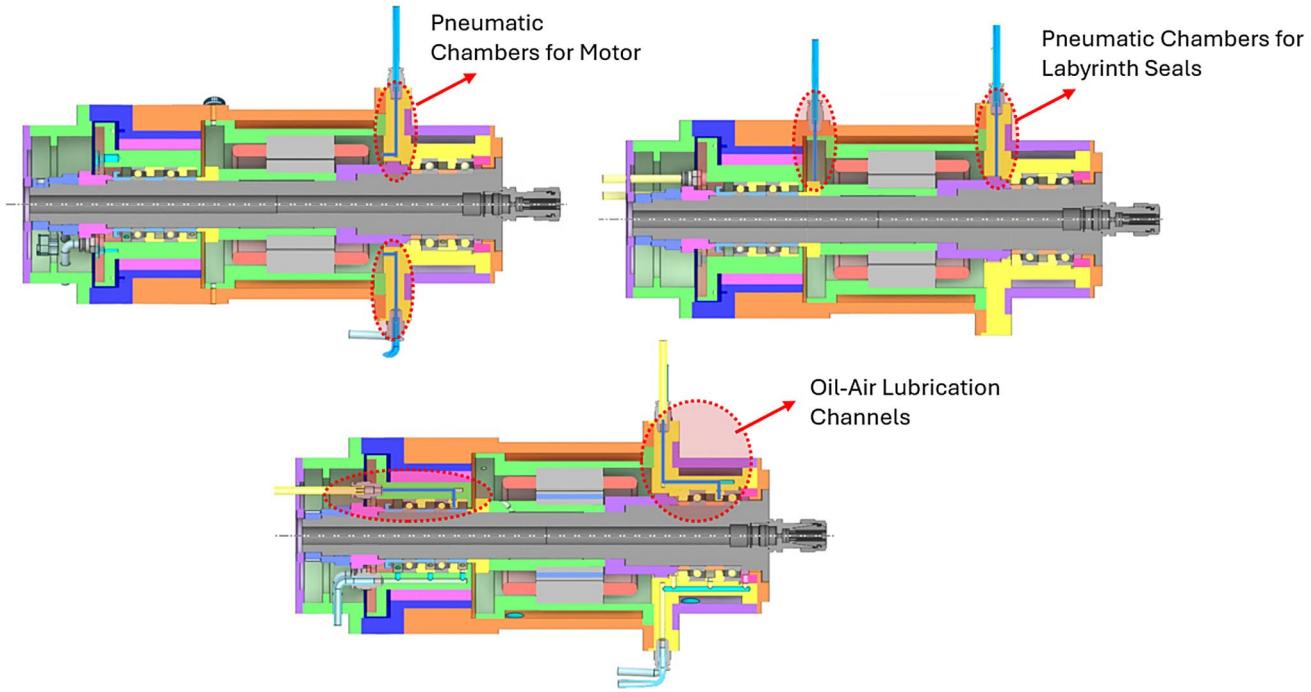

Fig. 13 Pneumatic and oil–air lubrication channels

of mass flow rate, provided as a tabular input for sensitivity studies. The reference temperature for convection is taken as the bulk air temperature obtained from the corresponding 1D thermal-fluid channel. During thermal optimization, ANSYS may yield effective convection coefficients rather than explicit flow variables. To recover physically meaningful air consumption values, the jet convection model was analytically inverted:

$$\dot{m} = \left(\frac{h\, D^{0.4}}{K_0} \right)^{1/0.6} \tag{12}$$

where K_0 is a calibration constant derived from reference CFD-based calculations. This inverse relationship allows the conversion of optimized convection coefficients (W/mm²K) into equivalent mass flow rates (kg/s), facilitating: Verification against pneumatic system capabilities, Comparison of cooling effectiveness between bearing groups, and trade-off analysis between thermal performance and air consumption.

Reduced Order Model with POD-based Thermal Modal Analysis:

To further reduce computational costs, a Proper Orthogonal Decomposition (POD) framework is employed. CFD simulations are conducted for selected operating points, and spatial fields such as $h(x)$ or segment-wise UA values are collected as snapshots. POD is then used to extract dominant thermal modes, enabling rapid reconstruction of boundary conditions for new operating points without additional CFD simulations. The reconstructed thermal boundary conditions are subsequently applied within the transient thermal model, combining CFD-level accuracy with the efficiency of reduced-order modeling.

3 Optimization

The analytical modules presented in the previous section represent various competing behaviors in high-speed spindles. Based on these dynamic and thermal models, an optimization engine is constructed as illustrated in Fig. 14.

A multi-objective optimization scheme was developed to identify well-performing design variants at different stages of the spindle design process, helping evaluate inherent trade-offs and acting as a decision-making tool. The Teaching Learning Based Optimization (TLBO) algorithm, a population-based meta-heuristic introduced by Rao et al. [23], was employed as the core optimization engine. To handle multiple objectives and to extract Pareto-optimal solutions, the non-dominated sorting and niche-preservation mechanisms of NSGA-III [24] were integrated into the TLBO framework.

3.1 Early-Stage Optimization: Shaft Layout and Bearing Selection

A representative multi-objective optimization problem was formulated (Eq. 13) for early spindle design, focused on shaft layout, bearing selection, and conformance with core performance targets, prior to the inclusion of auxiliary spindle components and the cooling system. While such decisions are typically made using experience-driven conventions in industrial design settings, the goal here is to further explore these conventions and their underlying trade-offs across feasible bearing configurations, adding a layer of clarity and verification to existing knowledge on early spindle design development.

$$\begin{aligned} &\text{Min } J_1 : 1/(\omega_1/1000) \\ &\text{Min } J_2 : 1/(\omega_2/1500) \\ &\text{Min } J_3 : \delta_{running}/1000 \\ &\text{Min } J_4 : 1/(L10/1 \times 10^{-7}) \\ &\text{s.t } 10 < X1 < 30 \\ &\quad 150 < X2 < 250 \\ &\quad Light < X3 < Medium \end{aligned} \tag{13}$$

The shaft layout is shown in Fig. 15. The bearing type (ACBB), orientation (O-configuration), and the total shaft length (350 mm) were fixed as a preliminary decision. Seven feasible bearing configurations (Fig. 16) were considered from SKF catalogue [25], spanning different bearing inner ring diameters (XX07, XX08, XX09 → 35 mm, 40 mm, 45 mm), contact angles (CE, ACD → 15°, 25°), and bearing designs (71XXX, 70XX → compact spindle bearings with small ball size, standard bearings). SKF bearings were opted for complete parameter availability; thus, the results are to be interpreted as representative rather than

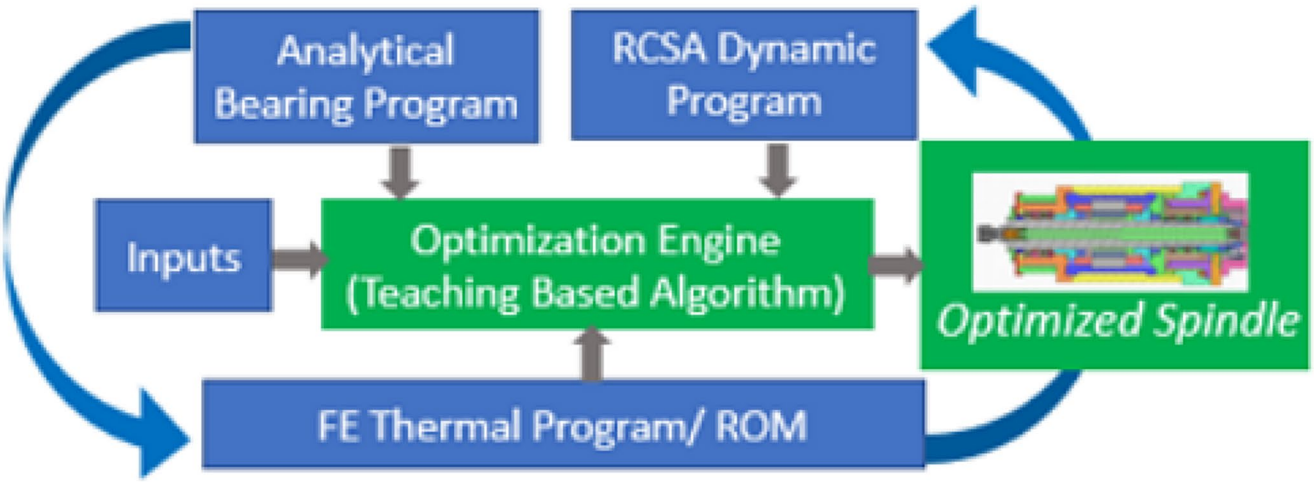

Fig. 14 Optimization scheme

Fig. 15 Shaft Layout

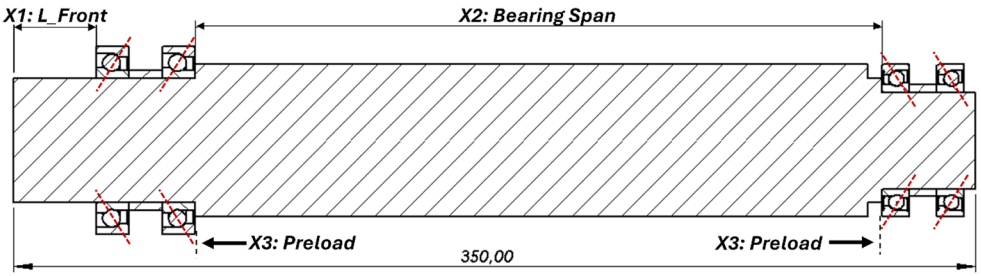

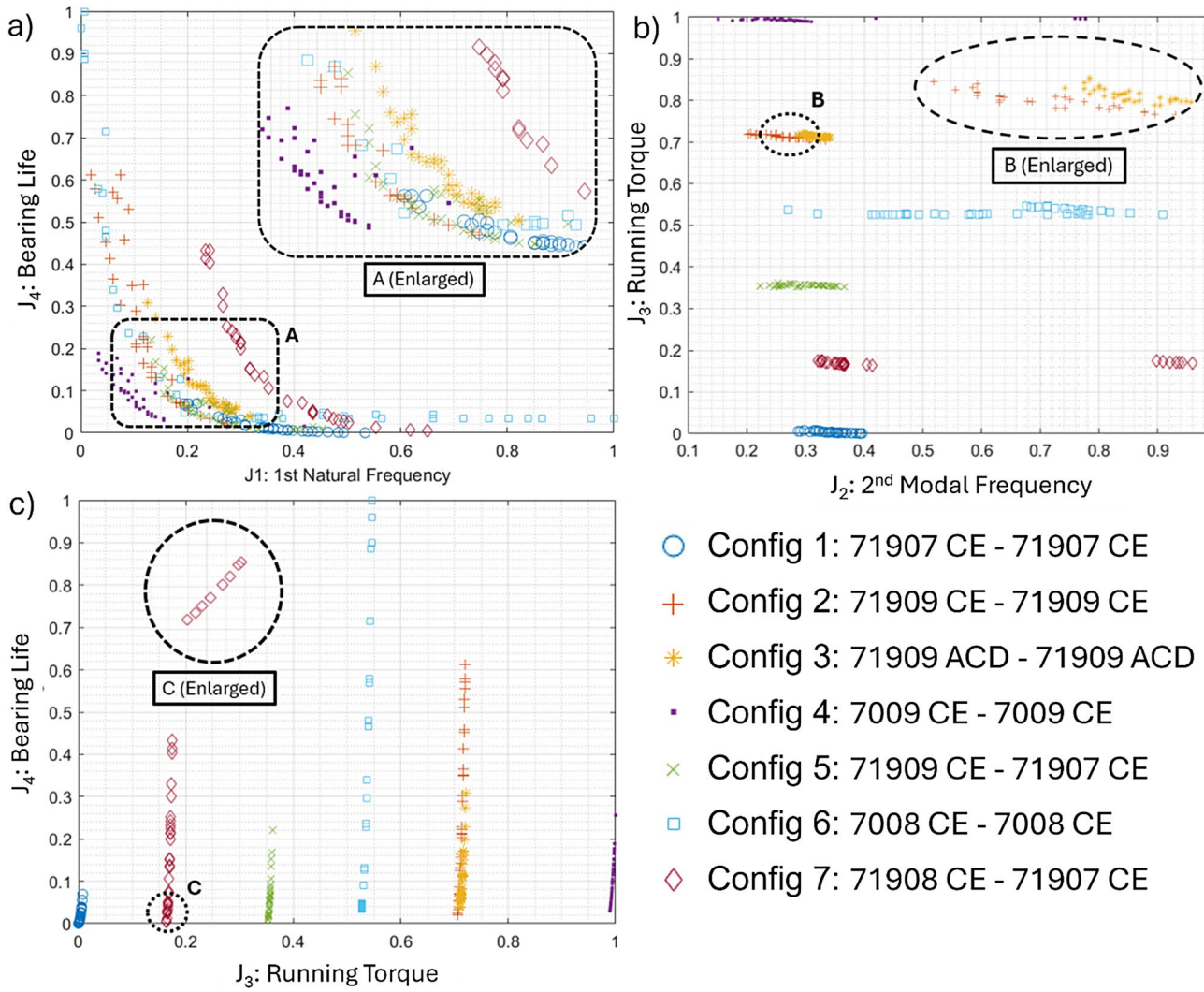

Fig. 16 Bearing Selection Pairs and Performances

brand-specific. The selected configurations also satisfied minimum shaft diameter requirements from the critical-speed study (Fig. 4). For each bearing configuration, the respective light-to-medium preload classes were considered in compliance with high-speed spindle requirements.

Four normalized objectives were minimized. In Eq. 13, J_1 and J_2 are the inverse of the 1st and 2nd FRF modal frequencies (ω_1 and ω_2, respectively), representing the fundamental dynamic rigidity at low frequencies and higher bending modes. J_3 is the total bearing running torque ($\delta_{running}$), which served as a proxy for heat generation. Bearing running torque was estimated using manufacturer-recommended formulations, detailed in our previous work [26]. J_4 is the inverse of the standard L10 bearing life metric [27], which was computed based on catalogue parameters under a preload-dominated loading condition.

The multi-objective optimization problem in Eq. 13 was solved independently for each bearing configuration. Each

simulation was run with a population size of 50 for 50 iterations, which was confirmed beforehand to yield results with acceptable convergence.

3.1.1 Results and Discussion

Each configuration produced a non-dominated population of 50 Pareto optimal solutions. Due to the high-dimensional nature of the solution set, the key Pareto fronts are shown in Fig. 16 with normalized objective function values (lower values are better).

Figure 16a shows the expected rigidity–life compromise. Higher rigidity generally reduces bearing life, aligning with standard design convention. Interestingly, it was observed that multiple configurations achieved similar trade-offs within a narrow band, allowing significant design freedom with respect to the concerned design objectives. This Pareto plot also allowed swift decision-making regarding poor-performing configurations. Configuration 7, for instance, is not stiff enough despite having a preferable contact angle and bearing design. Figure 16b addresses the dynamic–thermal trade-off: opting for designs with higher modal frequency also increases running torque, and therefore, poor thermal performance. Torque levels differ markedly across bearing configurations while exhibiting similar rigidities, highlighting the importance of proper bearing selection. Comparing configurations 2 and 3 demonstrates that low contact angle bearings significantly outperform high contact angle bearings in terms of rigidity while also generating slightly lower torque. Figure 16c indicates that within a configuration, torque and life can often be improved simultaneously through appropriate parameter selection, despite clear torque separation between configurations.

To support configuration-level selection, the colormap in Fig. 17 summarizes the objective-wise mean values of the Pareto-optimal solution sets for each bearing configuration (darker tones indicate better performance). Configurations 1 and 5 exhibit the most favorable overall behavior, whereas the remaining configurations can be excluded due to significant degradation in at least one objective. Configuration 1 shows comparatively better thermal performance and bearing life, while Configuration 5 provides superior dynamic performance with acceptable penalties in the remaining objectives. Based on the dynamics-focused design priority of this study, the inclusion of a modular cooling system in subsequent iterations, and the balanced performance of Configuration 5 across all objectives, Configuration 5 was selected for subsequent design stages. It is noted that alternative, more systematic selection criteria, such as weighted aggregation or decision-making metrics, could also be adopted depending on application-specific priorities and customer requirements. However, for the authors' purpose, the above reasoning provided sufficient evidence to finalize a decision.

Table 4 lists representative Pareto-optimal solutions within Configuration 5, providing alternative reference combinations of the design parameters for subsequent design stages. These solutions were not intended to fix final design parameters, but rather to guide downstream decisions. In particular, the final layout was guided to remain close to

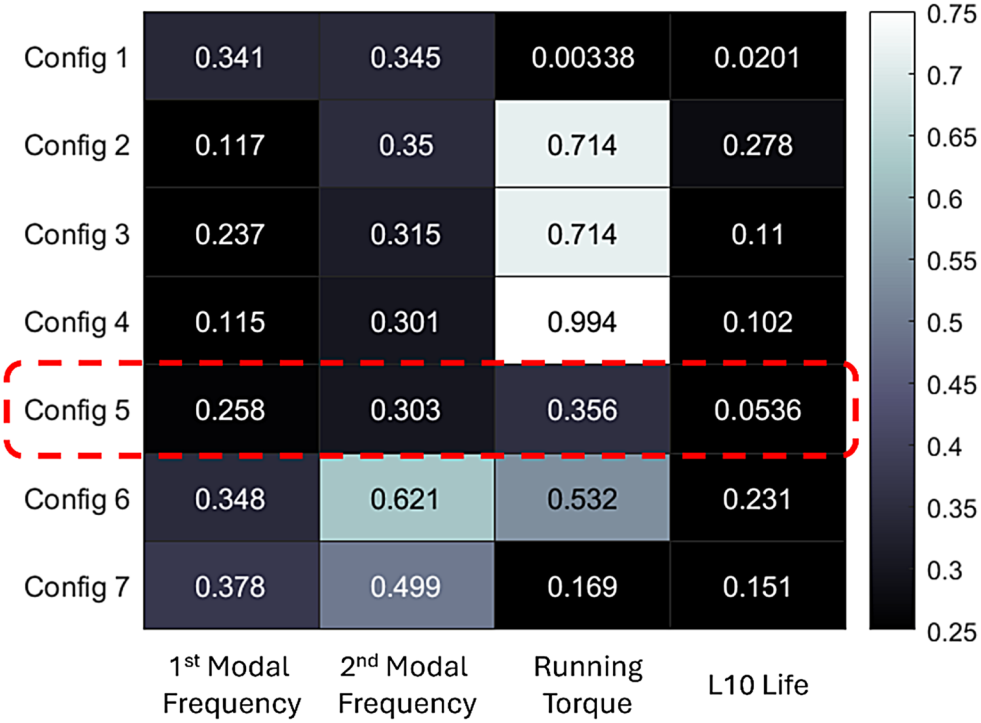

Fig. 17 Configuration Selection Colormap

Table 4 Pareto optimal solutions

Solution ID	X_1: Front Bearing Location (mm)	X_2: Bearing Span (mm)	X_3: Preload (*N*)
3	23	174	147
18	10	178	100
45	28	172	160

Solution 3 in terms of bearing locations (X_1: 24 mm, X_2: 178 mm), while preload was fine-tuned in later iterations due to its high sensitivity to bearing design, manufacturing tolerances, and assembly considerations.

More broadly, this optimization-based framework demonstrates its value as a decision-support tool for early spindle design, where multiple feasible layouts must be compared under competing performance requirements. Rather than prescribing a single optimal solution, the approach enables designers to identify robust design regions, reject unfavorable configurations early, and carry forward physically meaningful reference solutions into subsequent design stages.

3.2 Optimization for Manufacturing

Once the shaft layout is finalized during the early design stage, the next step in the design process is to add the necessary auxiliary components, like sleeves and locknuts to achieve a functional design. Although the spindle layout is largely fixed by this point, the dimensions of these auxiliary components offer reasonable flexibility to improve performance characteristics [7]. Utilizing the sensitivity analysis methodology as shared in [7], the multi-objective optimization problem in Eq. 14 was formulated for the intermediary spindle design iterate shown in Fig. 18. This stage therefore serves as a refinement step that complements the fundamental shaft–bearing optimization by extracting additional performance gains without altering the primary design architecture.

The objective function matrix, *J*, in Eq. 14, considers two objectives: J_1, the inverse of the 1st FRF modal frequency (ω_1), representing general dynamic performance; and J_2, the total mass of the shaft-bearing unit, a preferred design objective for lightweight spindle configurations. The design variable matrix, *X*, comprises six dimensions identified as sensitive to both objectives: front stepped sleeve length, motor shoulder diameter, motor sleeve diameter, rear stepped sleeve length, rear stepped sleeve diameter, and tail length. The box constraints for these parameters were set with space and manufacturability constraints in mind. It is also emphasized that extensive optimization was not pursued at this stage, as the bulk of the spindle performance was already determined; auxiliary components primarily provide an opportunity for incremental refinement of system dynamics.

$$
\begin{aligned}
&\text{Min } J(1) : 1/\omega_1 \\
&\text{Min } J(2) : mass \\
&\text{s.t } 5.75 < X(1) < 12 \\
&\quad 53 < X(2) < 65 \\
&\quad 53 < X(3) < 65 \\
&\quad 45 < X(4) < 70 \\
&\quad 10 < X(5) < 20 \\
&\quad 0 < X(6) < 150
\end{aligned}
\tag{14}
$$

The multi-objective optimization problem in Eq. 14 was run with a population size of 25 and for 30 iterations, yielding a solution set comprising a singular design point, shared in Table 5. The nominal values were chosen by the authors based on conventional design sense before optimization. The results show notable improvements of 7% and 11% in both objectives, respectively, for this design iteration. It was interesting to see the convergence of all parameters to their lower limits, pointing towards their seemingly monotonic behavior. However, this was not observed during the pre-optimization sensitivity analysis and manual tuning efforts by the authors, where the nominal design point was the reference point for perturbations in the design space. This highlights the benefit of using optimization techniques for such problems. The clean convergence of the solution set indicates that no pronounced trade-off between natural frequency and mass exists within the considered auxiliary design space. Based on this result, the authors also share the following as general spindle design conventions: 1) the bulkiness of the middle section of the shaft should preferably be minimized within safety limits, and 2) spindle tail

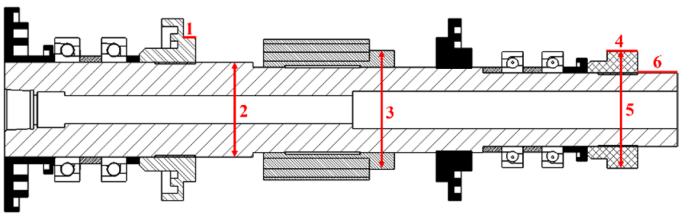

Fig. 18 The dimensions for iterative spindle design and optimization

Table 5 Design point after optimization

	X_1 (mm)	X_2 (mm)	X_3 (mm)	X_4 (mm)	X_5 (mm)	X_6 (mm)	Dominant Natural Frequency (Hz)	Mass (kg)
Nominal	8	60	60	55	15	20	965	5.55
Optimal	5.7	53	53	45	10	0	1035 **(↑7%)**	4.95 **(↓11%)**

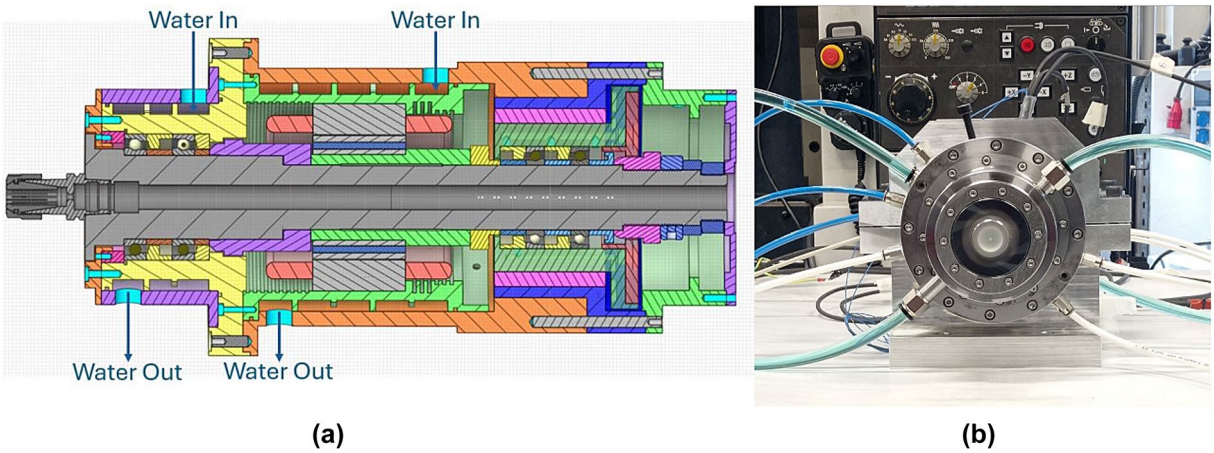

Fig. 19 **a**) Cross-sectional view of water-cooling circuit, **b**) External connections in final prototype

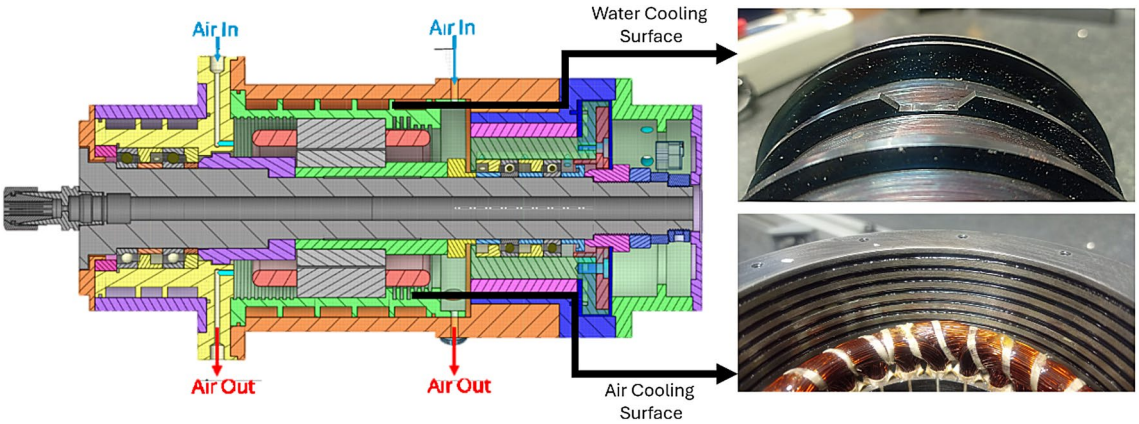

Fig. 20 Cross-sectional view of air-cooling circuit and respective components

tuning efforts should also consider decreasing the tail length in addition to elongation.

The dimensions in Table 5 were adapted in the final design, except for the tail section, which was slightly elongated to 30 mm in future iterations to accommodate functional components like the encoder. Beyond these incremental improvements, further performance gains are expected to depend primarily on thermal management strategies and operating conditions, which are addressed in the subsequent sections.

3.3 Thermal Sensitivity and Energy-Aware Cooling Considerations

Following the optimization-guided refinement of auxiliary components, the next stage in the spindle design focused on the cooling system design. This section outlines the salient cooling design features and a thermal sensitivity analysis with respect to variable cooling parameters.

3.3.1 Cooling and Pneumatic System Design

For MRL-40 K, the cooling system was designed in a modular way, with separate subsystems targeting the front bearings and motor chamber. This modular cooling system design concept has the potential to improve energy efficiency and thermal performance as the zonal cooling load can be managed according to real-time requirements [28]. Generally, the heat generation profiles for the motor and bearings are different due to different underlying physical mechanisms, which means that in a single-circuit passive cooling system, one zone may be under- or over-cooled. Figure 19 shows the relevant cross-sectional view and manufactured system.

The quasi-parallel channel design shown in Fig. 19 was finalized to minimize pressure drop. The fin dimensions were optimized via FE simulations to maximize heat transfer efficiency. A high surface roughness of 100 microns was maintained at heat transfer surfaces to improve efficiency. Figure 20 indicates the surfaces with an intentionally rough finish.

Table 6 Temperature and mass flows limits and results

		$T_{Bearing}$ (°C)	T_{Motor} (°C)	$\dot{m}_{front}$ (kg/s)	$\dot{m}_{rear}$ (kg/s)	$\dot{m}_{motor}$ (kg/s)	$\dot{m}_{laby\_front}$ (kg/s)	$\dot{m}_{laby\_rear}$ (kg/s)
Range	Lower Value	21	21	0.001	0.001	0.00325	0.00325	0.00325
	Upper Value	25	25	0.002	0.002	0.004	0.004	0.004
Pearson Coefficient	Average Temperature	0.66	0.64	−0.13	−0.27	−0.30	−0.12	−0.12
	Thermal Expansions	0.15	0.93	−0.05	−0.29	−0.32	−0.12	−0.12

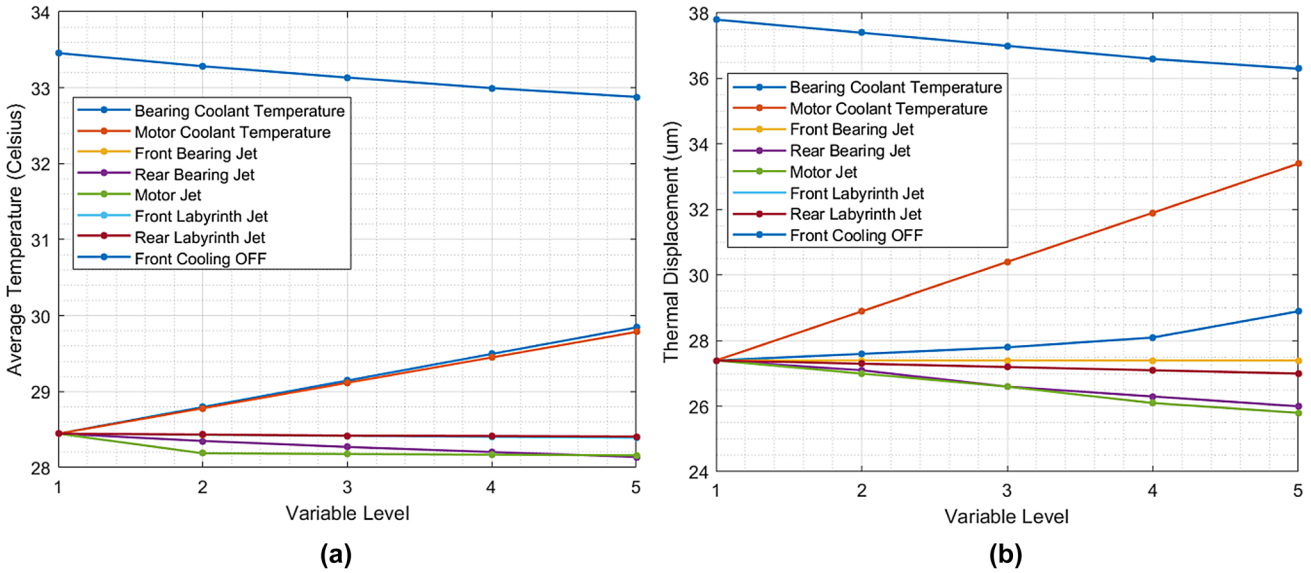

Fig. 21 Sensitivity of Thermal Parameters

For the internal volume of the motor chamber, a pneumatic system was designed to maintain air flow for cooling via the inlet and outlet points indicated in Fig. 20. Thus, the motor cooling jacket also features cooling fins on its internal surface. The fin dimensions are optimized for maximum forced convection coefficient. As with the water-cooling surfaces, the roughness of air-cooling surfaces was also kept high for maximum heat transfer.

3.3.2 Thermal Sensitivity

The cooling system design described in the previous section incorporates multiple water and air inlets that can be optimized for sustainable thermal management. In practice, however, spindle thermal behavior is governed by a combination of localized heat generation, convective cooling effectiveness, and operating constraints, many of which offer limited independent controllability. As a result, aggressive multi-objective optimization of thermal parameters does not necessarily lead to meaningful design improvements once baseline cooling requirements are met. Accordingly, the present study adopts a sensitivity-driven approach to examine the relative influence of key thermal management parameters on spindle temperature levels and thermally induced shaft expansion.

In this approach, one variable was varied while all others were held fixed at their nominal values. For each parameter, the lower and upper bounds of the variation range are summarized in Table 6, and five equally spaced levels were evaluated. The resulting trends are illustrated in Fig. 21, and the corresponding Pearson correlation coefficients are reported in Table 6.

The results in Fig. 21a show that the average spindle temperature is most strongly influenced by the bearing and motor coolant temperatures. Increasing either coolant temperature leads to a near-linear rise in average temperature. This indicates that, as a whole, both cooling circuits are equally important for overall thermal management and spindle health. In contrast, increasing the mass flow rates associated with bearing, motor, and labyrinth oil jets leads to modest temperature reductions, with the rear bearing and motor jets exhibiting the strongest cooling effect among these parameters. The comparatively weak sensitivity of the labyrinth jets indicates that their contribution to thermal control is limited. Overall, these trends confirm that coolant boundary conditions dominate the average thermal state, while lubrication-related convection primarily plays a secondary role.

Figure 21b presents the sensitivity of axial thermal displacement, which varied between 26 and 33 μm. In this case, motor coolant temperature is the most dominant factor,

exhibiting a strong positive correlation of 0.93 with thermal expansion. This behavior is physically consistent as the motor region contributes significantly to the overall thermal growth of the spindle shaft. Bearing coolant temperature shows a noticeably weaker influence on expansion, possibly because of its smaller size compared to the motor and the extra convective cooling effect produced by the oil-air mist circulation. Increasing bearing and motor jet mass flow rates generally reduce thermal displacement, with rear bearing and motor jets again showing the most pronounced impact among the lubrication-related parameters. Since there is no dedicated cooling system for the rear bearing set, this trend is expected. Similar to the temperature results, the labyrinth jets have minimal influence on thermal expansion within the considered design space.

A separate simulation was also run where the front bearing mass flow rate was varied while the bearing cooling circuit was turned off. As expected for both cases, the average temperature and the thermal expansion grew significantly. However, it was observed that the sensitivity of mass flow rate to the thermal performance was much stronger in the absence of bearing cooling. This points towards a possible trade-off between the coolant temperature and mass flow rate settings, where a more efficient cooling system may be feasible to use by tuning the oil-air lubrication jet accordingly. This was not further investigated in this work, however.

Overall, the sensitivity study highlights that global thermal metrics are primarily governed by coolant temperature levels, while oil-air jet parameters offer limited but consistent advantages as well.

4 Design Evolution & Manufacturing

Figure 22 illustrates the evolution of the spindle design from the initial concept to the final configuration, highlighting key modifications implemented to address dynamic, thermal, and manufacturing constraints via optimization. The design evolution is driven by an iterative optimization framework that integrates analytical bearing models, dynamic analyses, and FE–based thermal modal simulations. The progression shown in Fig. 22 reflects the trade-offs between high-speed performance, thermal stability, and manufacturability, and provides context for the practical design insights summarized in the following section.

The following observations may be useful for spindle designers and researchers as noted by the authors:

- Bearing manufacturers provide detailed guidelines for dimensional and form tolerances of spindle shafts and housing. However, centrifugal expansion at high speeds affects system dynamics; therefore, speed-dependent bearing fits should be considered. Industry experts recommend a slightly tighter inner ring–shaft fit and a looser outer ring–housing fit, noting the trade-off of increased stiffness and heat generation at low speeds.
- Bearing spacers should be designed in a floating configuration with a high surface finish to prevent imbalanced loading in tandem bearing sets.
- The number of threaded shaft components should be minimized to avoid non-uniform contact. Accordingly, the initially designed front and rear preload locknuts were revised by removing the front locknut based on industrial recommendations.
- The constant preload mechanism employs axially acting soft springs on the rear bearing set. As these springs influence both static and high-speed dynamics, their stiffness should be treated as a critical design variable and calculated to avoid over- or under-stiffening at operating speed.
- Finite element analyses showed that thermal gradients increase when bearing and motor radial dimensions are similar; thus, using smaller bearings with relatively larger-diameter motors improves heat dissipation.
- The rear bearing size, typically the smaller bearing, governs the shaft wall thickness and therefore limits the design of through-shaft cooling systems.
- Although smaller bearings and spindle components improve thermal management and dynamic balance, they increase lubrication system complexity:
    - Lubrication channels, nozzles, and drainage paths become smaller.

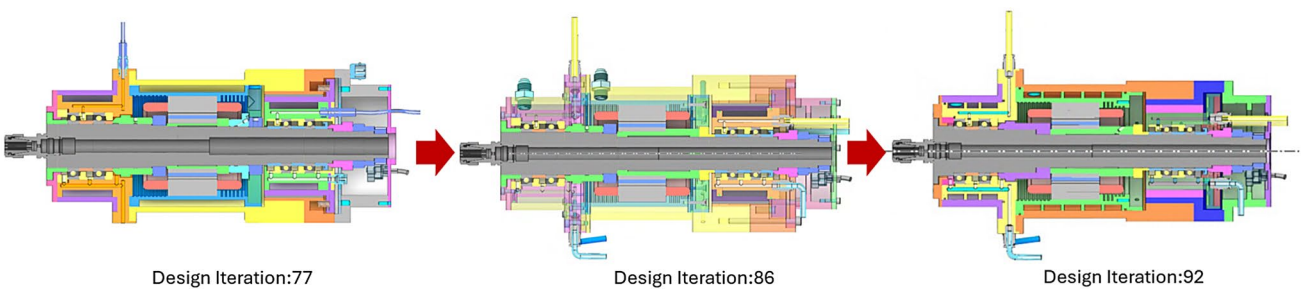

Fig. 22 Design evolution during the iterative spindle design and optimization process

Table 7 Experimental equipment

Equipment	Specifications	Tests
Laser Displacement Sensor	Keyence LK-H052K	Thermal expansion
Accelerometers	PCB Piezotronics 352C23 (5.63 mV/g)	Modal analysis
Impact Hammer	PCB Piezotronics 086C03 (11	Modal analysis
Thermocouples	OMEGA K-type/J-type thermocouples	Temperature growth

- Labyrinth seals and flinger/slinger features are required to prevent leakage, along with dedicated lubrication and drainage systems.
- Sliding or mobile elements in spring preload systems complicate lubrication and cooling channel design; in this study, lubrication channels were integrated into the sliding elements to minimize leakage.

5 Experimental Verification

Although the spindle was originally designed for a maximum operating speed of 40,000 RPM, an error in the selection of the encoder resolution limited the achievable control precision at high speeds. As a result, stable and accurate spindle control could only be maintained up to approximately 25,000 RPM. To ensure reliable operation and measurement accuracy, all experimental tests presented in this study were therefore conducted at spindle speeds of up to 25,000 RPM.

A dedicated clamp-type testbed with a heavy base bolted to a machine tool table was constructed to conduct experimentation. A range of experiments was conducted on the manufactured MRL-40 K prototype to evaluate its performance against the set benchmarks. It is pertinent to note here that the testing was performed up to 25,000 RPM.

Table 7 lists the equipment used for experimentation and the types of experiments conducted.

5.1 Dynamic Performance

To assess the dynamic performance of the manufactured prototype, impact hammer testing was performed to acquire the direct frequency response function (FRF) at the spindle tip. The FRF is a core indicator of the rigidity of the spindle under cutting loads at high speeds.

Initially, impact tests were conducted in the free-free condition (Fig. 23a) by suspending the spindle from a platform to identify the fundamental modes of the structure. In this configuration, no clearly distinguishable FRF modes were observed, as seen in Fig. 23b, indicating a highly rigid structure. To obtain a more representative dynamic response, a dummy tool was introduced, resulting in a pronounced response in the 900–1100 Hz frequency range.

It is noted that two closely spaced and strongly coupled modes appear within this range. Reverse identification was, therefore, not pursued as a reliable separation of the isolated spindle mode was not feasible with sufficient confidence. Based on modal characteristics and relative amplitudes, the first peak at 882 Hz is attributed primarily to tool-dominated bending, whereas the second peak at 1150 Hz is interpreted as a shifted representation of the first spindle natural frequency. This observation is generally consistent with the optimization results reported in Table 7.

Figure 23b also indicates that there are two fundamental modes at ~3000 Hz and ~4300 Hz, with magnitudes below 4×10^{-8} m/N. These are healthy values for the higher-order modes of a machine tool spindle and meet the dynamic performance criteria in Table 2.

Similar impact testing was also conducted for the axial direction. Figure 24 shows the direct FRFs obtained in the axial direction at the spindle tip. A dominant axial resonance is observed at approximately 360 Hz, which is primarily associated with a rigid-body-dominated axial mode of the shaft–bearing system governed by axial bearing stiffness and preload. Although this frequency lies close to the rotational frequency at 21,600 RPM, axial excitation during cutting is limited compared to radial loading. Consequently,

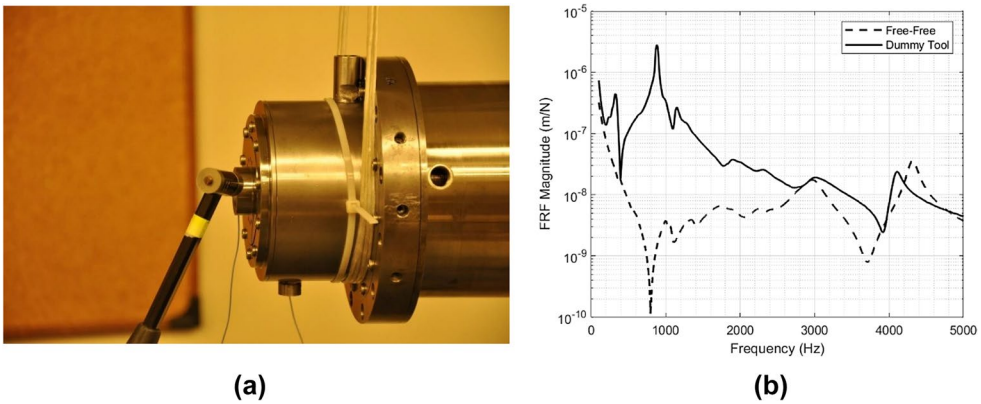

Fig. 23 **a**) Impact testing setup (free-free condition), **b**) Free-free FRF in radial direction

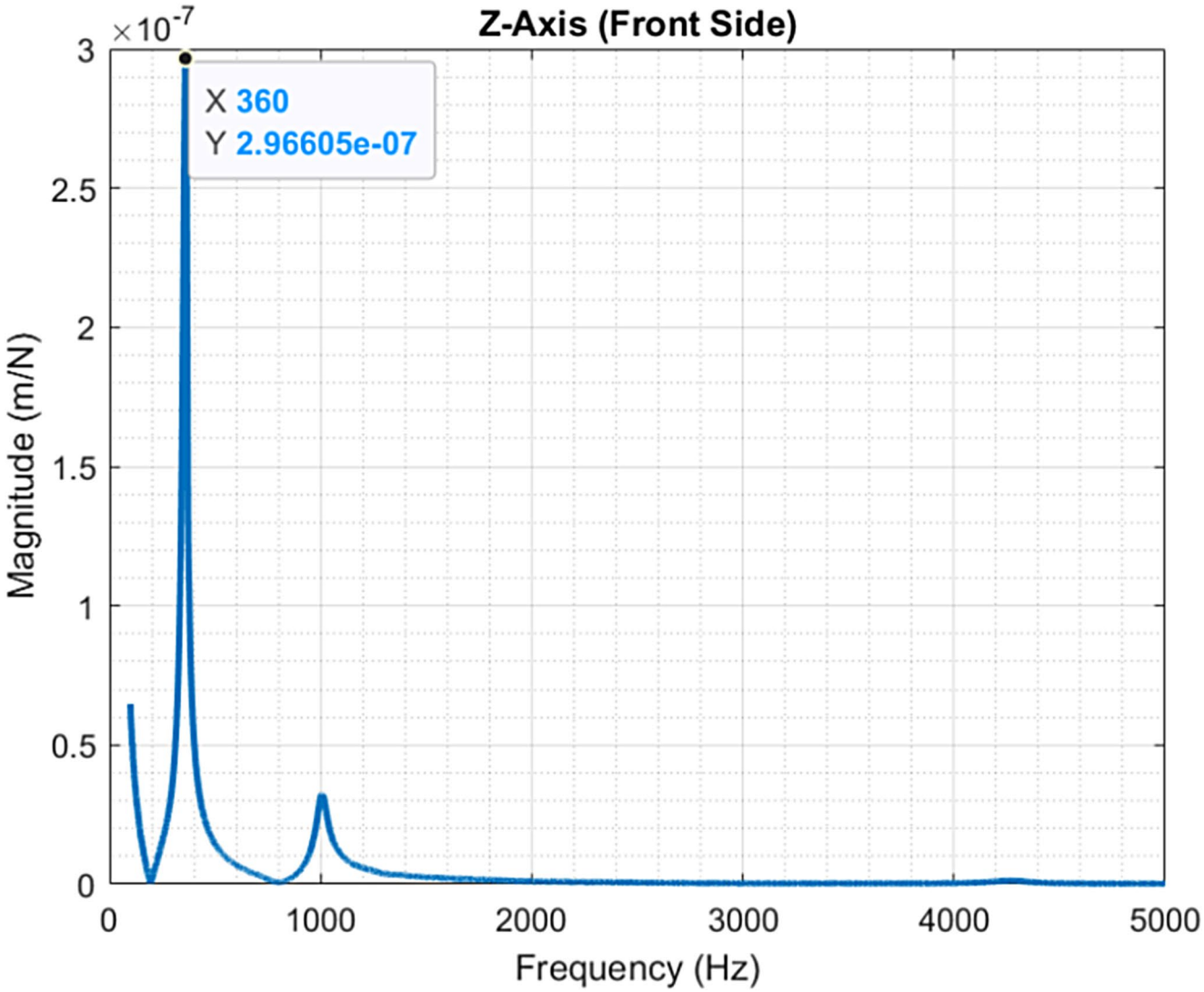

Fig. 24 Shaft FRF in axial direction

this mode is not expected to be critically excited under normal operating conditions and is interpreted as a qualitative indicator of axial stiffness rather than a limiting factor for spindle performance.

5.2 Thermal Testing

Thermal expansion at the spindle tip was measured using a laser sensor for long-duration runs. The spindle was run in increments of 5,000 RPM up to 25,000 RPM, for 20 min at each speed, allowing ample time for the thermal response to reach a steady state. Figure 25 summarizes the thermal expansion results. The raw measurements from the sensor, shown in black, indicated a displacement of 53 µm at the end of the test.

It was observed that a significant part of this axial motion came from non-thermal axial drift at higher speeds. This was confirmed by performing multiple ramp-up tests from 0 to 25,000 RPM at a near isothermal state (5-minute test duration). It was observed that the shaft displaced axially up to 26.4 µm at 25,000 RPM without thermal expansion. Therefore, the raw measurements in Fig. 25 were compensated by removing the average axial drift recorded at each speed range. The red line in Fig. 25 shows the compensated result along with the compensation values. After compensation, the maximum thermal elongation was recoded as ~29 µm at 25,000 RPM, which is a healthy value for high-speed spindles and within the target set in Table 2.

The axial drift phenomenon is speculated to be due to dynamic forces developing in the shaft-bearing assembly at elevated speeds and has been previously reported for ultra-high-speed spindles [29]. The authors propose that the following reasons may contribute to this unwanted motion:

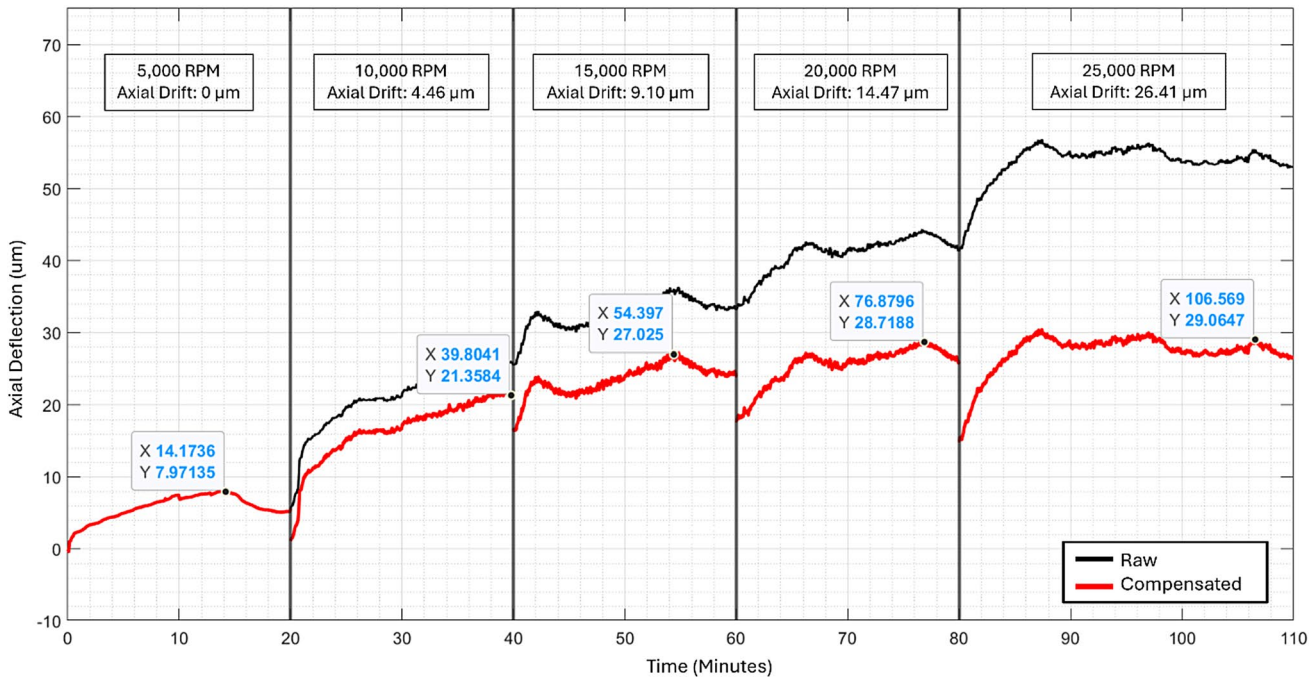

Fig. 25 Thermal expansion measurement

- Changing bearing geometry and contacts at high speed under centrifugal and gyroscopic effects.
- Speed-dependent radial forces are partially transmitted along the axis and consequently cause the soft preloading springs to deform.
- Irregularities in bearing geometry at high speeds [29].
- Incorrect design, manufacturing, or assembly of a component(s) in the bearing preload circuit.

5.3 Temperature Growth

The thermal performance of MRL-40 K was evaluated by measuring temperature rise at key locations using thermocouples (Fig. 26), with speed increments of 5,000 RPM from 0 to 25,000 RPM in 30-minute intervals. Figure 26 shows that the front side and motor housing, with targeted cooling for the bearings and toolholder, maintained better thermal stability than the rear, which does not feature localized cooling. This is an intentional design feature to prioritize sustainable and efficient thermal management in spindle zones near the cutting tool while allowing higher but safe temperatures at the rear, where higher temperature gradients are affordable. Although internal temperatures near the bearings could not be measured directly, the measured surface temperature of 35 °C was well within the 40 °C target. Moreover, the measured temperature trends are consistent with results reported in recent data-driven and optimization-based studies on spindle thermal behavior [30, 31], supporting their relevance in thermal management scenarios.

6 Conclusions

The design and optimization of a 40,000 RPM high-speed machine tool spindle were presented in this work. A key contribution is the introduction of an integrated optimization framework that couples fast yet physically representative dynamic and thermal models using the Teaching–Learning-Based Optimization (TLBO) algorithm. The dynamic behavior of the spindle was efficiently captured using an analytical bearing model and a Timoshenko-beam shaft representation, solved through Receptance Coupling Substructure Analysis (RCSA). This approach avoided repeated FE solutions and enabled rapid evaluation of dynamic constraints such as stiffness, stability, and critical speeds within the optimization loop. In parallel, a POD-based thermal modal simulation was employed to predict transient thermal behavior with sufficient accuracy, while maintaining computational efficiency. The combination of these models allowed simultaneous consideration of thermal–dynamic coupling effects, which are dominant in high-speed spindle operation.

Beyond performance optimization, manufacturability considerations including bearing fits, preload mechanisms, lubrication and cooling layouts, sealing strategies, and

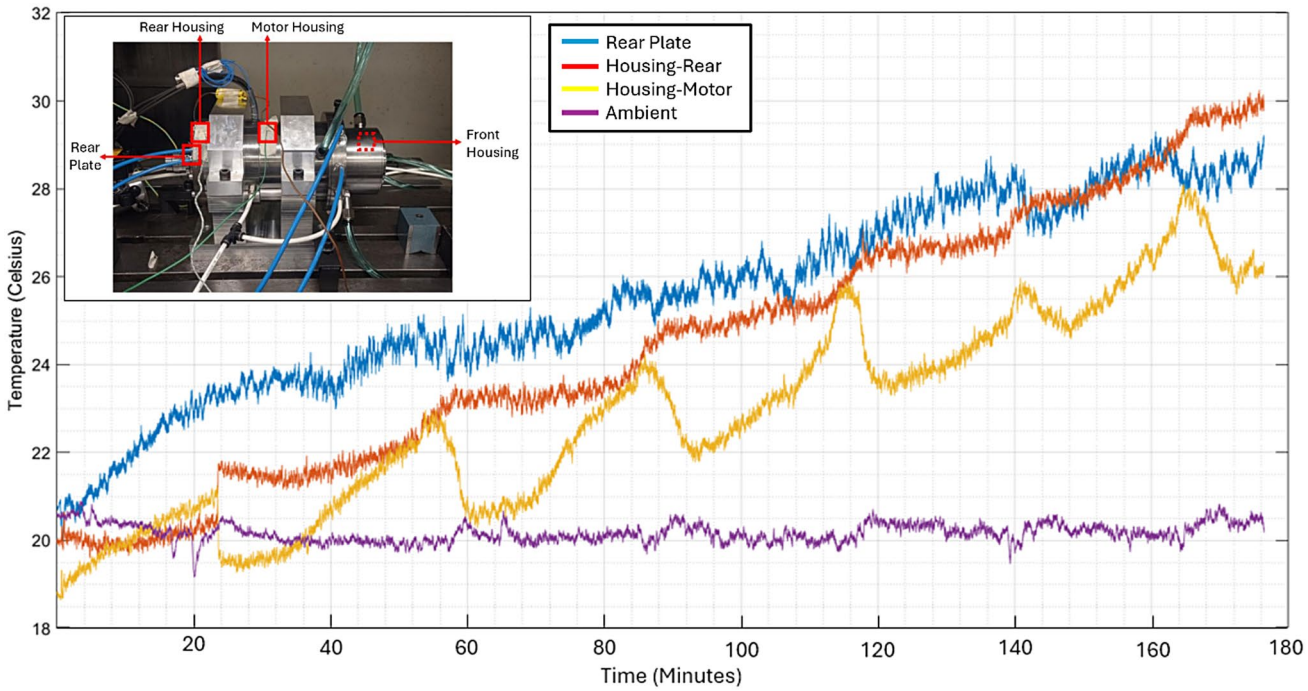

Fig. 26 Temperature growth measurement

component integration, were explicitly incorporated and discussed in the context of spindle design. The resulting spindle architecture reflects realistic industrial constraints and highlights the importance of accounting for manufacturing feasibility early in the optimization stage. Sensitivity analyses further support informed trade-offs between thermal performance, dynamic stability, and system complexity.

Although the spindle was designed for a maximum speed of 40,000 RPM, a limitation in the encoder resolution restricted precise control to 25,000 RPM. Consequently, experimental validation was conducted up to 25,000 RPM, ensuring stable operation and reliable measurements. Despite this limitation, the experimental results confirm the validity of the proposed modeling and optimization framework, demonstrating consistent dynamic and thermal behavior with analytical predictions.

To the authors' knowledge, this work represents one of the first studies to present a fully manufactured and experimentally tested high-speed spindle developed using a unified, multi-objective optimization framework that integrates dynamic modeling, reduced-order thermal analysis, manufacturability considerations, and experimental validation. The proposed methodology provides a transferable and scalable template for the design of high-speed spindles under realistic industrial constraints and can be extended to future studies involving higher operating speeds, advanced cooling strategies, or operational optimization.

Supplementary Information The online version contains supplementary material available at https://doi.org/10.1007/s40684-026-00860-2.

Acknowledgements We would like to acknowledge the financial support provided by TÜBİTAK (Project No. 120N896). The practical assistance and technical consultation of our industrial partners - MAXIMA, EUROSERVO, and AKIM METAL - are also duly acknowledged.

Funding Open access funding provided by the Scientific and Technological Research Council of Türkiye (TÜBİTAK).

Data Availability The authors declare that data collected and analyzed during this study is available in this article. Raw data used to support the analysis is available from the corresponding author on reasonable request.

Declarations

Conflict of interest The authors declare no competing financial or non-financial interests.

References

1. Abele, E., Altintas, Y., & Brecher, C. (2010). Machine tool spindle units. *CIRP Annals*, *59*(2), 781–802.
2. Denkena, B., Bergmann, B., & Klemme, H. (2020). Cooling of motor spindles—a review. *The International Journal of Advanced Manufacturing Technology*, *110*(11), 3273–3294.
3. https://www.step-tec.com/en/spindle-platforms/hvc-140.html
4. https://www.fischerspindle.com/en/products/milling-spindles
5. https://www.ibag.ch/en/product-filter.html
6. Mayr, J, Jedrzejewski, J, Uhlmann, E, Donmez, M. A, Knapp, W, Härtig, F, & Wegener, K. (2012). Thermal issues in machine tools. *CIRP Annals*, *61*(2), 771–791.
7. Afridi,S. A, Yuksel, E, Rivera, G, Hong, S. W, & Budak, E. (2025). Sensitivity analysis of rotating auxiliary components of a high-speed spindle shaft assembly. *The International Journal of Advanced Manufacturing Technology*, 141, 5819–5831 https://doi.org/10.1007/s00170-025-15948-3
8. Ting, G. C., Huang, K. Y., & Lee, Y. H. (2025). Development and experimental verification of precision miniature Ultra-High-Speed axial air turbine. *International Journal of Precision Engineering and Manufacturing*, *26*, 3301–3339. https://doi.org/10.1007/s12541-025-01306-6
9. Cao, Y., & Altintas, Y. (2007). Modeling of spindle-bearing and machine tool systems for virtual simulation of milling operations. *International Journal Of Machine Tools And Manufacture*, *47*(9), 1342–1350. https://doi.org/10.1016/j.ijmachtools.2006.08.006
10. Ertürk, A., Budak, E., & Özgüven, H. N. (2007). Selection of design and operational parameters in spindle-holder-tool assemblies for maximum chatter stability by using a new analytical model. *International Journal of machine tools and manufacture*, *47*(9), 1401–1409. https://doi.org/10.1016/j.ijmachtools.2006.08.016
11. Li, H., & Shin, Y. C. (2004). Integrated dynamic thermo-mechanical Modeling of high speed spindles, part 1: Model development. *Journal of Manufacturing Science and Engineering*, *126*(1), 148–158. https://doi.org/10.1115/1.1644545
12. Hong, S. W, Kang, J. O, & Shin, Y. C. (2002). Dynamic characteristics of indeterminate rotor systems with angular contact ball bearings subject to axial and radial loads. *International Journal of precision engineering and manufacturing, 3* (2), 61-71.
13. Zhou, B., Chen, G., Mao, J., et al. (2025). Enhancing spindle precision: Thermal error modeling with Multi-parameter optimization and energy consumption data. *International Journal of Precision Engineering and Manufacturing*, *26*, 1837–1853. https://doi.org/10.1007/s12541-025-01230-9
14. Li, K. Y., Hsieh, P. C., Wang, J. J., et al. (2023). Optimization control method of intelligent cooling and lubrication for a geared spindle. *International Journal of Precision Engineering and Manufacturing*, *24*, 1753–1769. https://doi.org/10.1007/s12541-023-00840-5
15. Schmitz, T. L., Davies, M. A., & Kennedy, M. D. (2001). Tool point frequency response prediction for high-speed machining by RCSA. *Journal of Manufacturing Science and Engineering*, *123*(4), 700–707.
16. Schmitz, T., Betters, E., Budak, E., Yüksel, E., Park, S., & Altintas, Y. (2023). Review and status of tool tip frequency response function prediction using receptance coupling. *Precision Engineering*, *79*, 60–77.
17. Lassila, T., Manzoni, A., Quarteroni, A., & Rozza, G. (2014). Model order reduction in fluid dynamics: Challenges and perspectives. *Reduced order Methods for Modeling and Computational Reduction*, *235*, 273.
18. Budak, E. (2006). Analytical models for high performance milling. Part I: Cutting forces, structural deformations and tolerance integrity. *International Journal of Machine Tools and Manufacture*, *46*(12–13), 1478–1488. https://doi.org/10.1016/J.IJMACHTOOLS.2005.09.009
19. Li, H., & Shin, Y. C. (2004). Analysis of bearing configuration effects on high speed spindles using an integrated dynamic thermo-mechanical spindle model. *International Journal of Machine Tools and Manufacture*, *44*(4), 347–364. https://doi.org/10.1016/j.ijmachtools.2003.10.011
20. Shigley, J. E., Mitchell, L. D., & Saunders, H. (June 1 ,1985). "*Mechanical engineering design"* (4th Ed.). ASME. *J. Mech., Trans., and Automation*. June 1985; 107(2): 145 https://doi.org/10.1115/1.3258702
21. Zhu, J., Ni, J., & Shih, A. J. (2008). "Robust machine tool thermal error modeling through thermal mode concept."ASME. *J. Manuf. Sci. Eng.* December 2008; 130(6): 061006. https://doi.org/10.1115/1.2976148
22. Peyret, R., & Taylor, T. D. (2012). *Computational methods for fluid flow*. Springer Science & Business Media.
23. Rao, R. V., Savsani, V. J., & Vakharia, D. P. (2011). Teaching–learning-based optimization: A novel method for constrained mechanical design optimization problems. *Computer-aided Design*, *43*(3), 303–315.
24. Deb, K., & Jain, H. (2013). An evolutionary many-objective optimization algorithm using reference-point-based nondominated sorting approach, part I: Solving problems with box constraints. *IEEE Transactions on Evolutionary Computation*, *18*(4), 577–601.
25. SKF Group. (2008). *SKF general catalogue 6000/I EN*. SKF Group.
26. Canh, T., Hwang, J., Shim, J., Oh, J. S., & Hong, S. W. (2020). Multi-objective optimization of machine tool Spindle-Bearing system. *International Journal of Precision Engineering and Manufacturing*, *21*. https://doi.org/10.1007/s12541-020-00389-7
27. International Organization for Standardization (2007). *ISO 281: Rolling bearings — Dynamic load ratings and rating life*, Geneva, Switzerland.
28. Huang, C. K., Chen, T. C., Li, K. Y., et al. (2025). Optimization of machine tool spindle cooling for enhancement of thermal prediction accuracy and energy efficiency. *International Journal of Precision Engineering and Manufacturing-Green Technology,* https://doi.org/10.1007/s40684-025-00738-9
29. Anandan, K. P., & Ozdoganlar, O. B. (2013). Analysis of error motions of ultra-high-speed (UHS) micromachining spindles. *International Journal of Machine Tools and Manufacture*, *70*, 1–14. https://doi.org/10.1016/j.ijmachtools.2013.02.005
30. Cheng, Y., Jin, S., Qiao, K., et al. (2025). Predictive modeling of thermal displacement for High-Speed electric spindle. *International Journal of Precision Engineering and Manufacturing*, *26*, 345–361. https://doi.org/10.1007/s12541-024-01101-9
31. Chaaibi, W., Matezo-Ngoma, E., & El Ouafi, A. (2025). Prediction of spindle thermal errors for Real-time compensation in CNC machine tools using neural networks and design of experiments. *International Journal of Precision Engineering and Manufacturing*, *26*, 3207–3222. https://doi.org/10.1007/s12541-025-01302-w